Global off-line evaluation of the ISBA-TRIP flood model.

B. DECHARME[(1)], R. ALKAMA[(1)], F. PAPA[(2)],

S. FAROUX[(1)], H. DOUVILLE[(1)], C. PRIGENT[(3)]

Corresponding Author : Bertrand Decharme
Météo-France, CNRM/GMGEC/VDR
42 av. G. Coriolis, 31057 Toulouse, France
E-Mail : bertrand.decharme@meteo.fr

(1) Centre National de Recherche Météorologique / Météo-France, Toulouse, France
(2) NOAA-CREST, City College of New York, New York, USA
Now at Institut de Recherche pour le Developpement IRD-LEGOS, Toulouse, France
(3) CNRS / Laboratoire d'Etudes du Rayonnement et de la Matière en Astrophysique, Observatoire de Paris, France

ABSTRACT

This study presents an off-line global evaluation of the ISBA-TRIP hydrological model including a two-way flood scheme. The flood dynamics is indeed described through the daily coupling between the ISBA land surface model and the TRIP river routing model including a prognostic flood reservoir. This reservoir fills when the river height exceeds the critical river bankfull height and vice-versa. The flood interacts with the soil hydrology through infiltration and with the overlying atmosphere through precipitation interception and free water surface evaporation. The model is evaluated over a relatively long period (1986-2006) at 1° resolution using the Princeton University 3-hourly atmospheric forcing. Four simulations are performed in order to assess the model sensitivity to the river bankfull height. The evaluation is made against satellite-derived global inundation estimates as well as in situ river discharge observations at 122 gauging stations. First, the results show a reasonable simulation of the global distribution of simulated floodplains when compared to satellite-derived estimates. At basin scale, the comparison reveals some discrepancies, both in terms of climatology and interannual variability, but the results remain acceptable for a simple large-scale model. In addition, the simulated river discharges are improved in term of efficiency scores for more than 50% of the 122 stations and deteriorated for 4% only. Two mechanisms mainly explain this positive impact: an increase in evapotranspiration that limits the annual discharge overestimation found when flooding is not taking into account and a smoothed river peak flow when the floodplain storage is significant. Finally, the sensitivity experiments suggest that the river bankfull depth is potentially tunable according to the river discharge scores to control the accuracy of the simulated flooded areas and its related increase in land surface evaporation. Such a tuning could be relevant at least for climate studies in which the spatio-temporal variations in precipitation are generally poorly represented.

1. Introduction

The land surface hydrology represents an active component of the climate system (Dirmeyer 2000, 2001; Douville 2003, 2004; Koster et al. 2000, 2002) and is likely to influence the water and energy exchanges at the land surface, the ocean salinity and temperature at the mouth of the largest rivers (Durand et al. 2010), and the climate at least at the regional scale (Gedney et al. 2000; Douville et al. 2000a, b; Molod et al. 2004, Lawrence and Slater 2007, Alkama et al. 2008). These land surface processes are parameterized in Continental Hydrologic Systems (CHSs). CHSs are composed by Land Surface Models (LSMs), which provide realistic lower boundary conditions of temperature and moisture in Atmospheric General Circulation Models (AGCMs), and now generally include River Routing Models (RRMs) which convert the runoff simulated by the LSMs into river discharge in order to transfer the continental fresh water into the oceans and then to close the global hydrological cycle.

At the global scale, many studies have focused on RRMs development (Vörösmarty et al. 1989, Liston et al. 1994, Miller et al. 1994, Hagemann and Dümenil 1998, Oki and Sud 1998, Arora and Boer 1999, Coe 1998, Ducharne et al. 2003). These models are generally based on simple budget equations representing the temporal variations of the water mass stored in each grid cell of a hydrological network determined according to the actual topography. This network is generally derived at coarse resolution (from 0.25° by 25° to 4° by 4°) except Coe's model (1998) that used a 5-minute resolution. The main difference between these simple linear reservoir models is related to the processing of the river flow velocity that can be parameterized as:

- constant in space and time (Oki and Sud 1998) or using basin scale uniform transfer coefficients (Ducharne et al. 2003)
- constant in time but spatially distributed according to various relationships with the topography (Miller et al. 1994, Hagemann and Dümenil 1998, Coe 1998) or with both the mean annual river flow and the topography (Vörösmarty et al. 1989, Liston et al. 1994)
- variable in space and time according to the topography, the river geomorphology and the river water height using the Manning (1891) formula (Arora and Boer 1999, Lucas-Picher et al. 2003, Ngo-Duc et al. 2007, Decharme et al. 2010)

Nevertheless, most of these models do not account for inland water bodies (Vörösmarty et al. 1989, Liston et al. 1994, Miller et al. 1994, Hagemann and Dümenil 1998, Oki and Sud 1998, Arora and Boer 1999, Ducharne et al. 2003) or consider them as static (Coe 1998) while their evolution and variability have an important impact on the Earth's climate system.

Water bodies can be separated in two categories: anthropogenic and natural. Man-made inundated surfaces include reservoirs, rice fields and agricultural irrigation while natural inundated areas are related to river flooding, lakes, large ponds, and wetlands (bog, fen, mire, marshes). They have a strong influence on the annual cycle of river discharges in both tropical and high-latitude areas that emphasize their relevance for water resource management (Coe et al. 2002; Coe et al. 2008; Decharme et al. 2008). They affect the overlaying atmosphere through their relatively high evapo-transpiration that enhances latent versus sensible heat exchange with the atmosphere (Krinner et al. 2003). Finally, through CO_2 and/or methane emissions, surface water bodies, especially wetlands, regulate the biogeochemical cycles that impact the climate evolution. Indeed, they are the world's largest source of methane and a major contributor to its inter-annual variability (Houweling et al. 1999; Matthews 2000;

Bousquet et al. 2006, Ringeval et al. 2010) and could have contributed significantly to global warming since pre-industrial time (Shindell et al. 2004). Hence quantifying the distribution and variations of surface water bodies over the global land surface is a key question regarding climate change in terms of hydrological impacts as well as methane emissions (Bousquet et al. 2006). Consequently, recent efforts have been made to represent natural inland water surfaces in CHSs. Gedney et al. (2004) used an implicit representation in a LSM without any dedicated surface reservoir in order to estimate the potential feedback of wetland methane emissions on climate change. Other studies have proposed simple explicit parameterizations of flooded areas prescribing the residence time of water into pre-dimensioned reservoirs (Coe 1998; Coe et al. 2002; Krinner et al. 2003; Guntner et al. 2007).

However, the recent development of new satellite observations and techniques (Alsdorf et al. 2007; Prigent et al. 2001, 2007; Papa et al. 2010a) shows that inland water bodies greatly vary in space and time and evolve with environmental and climate conditions. Some new modeling capabilities have been proposed to represent inland water bodies, or at least floodplains, at continental scale and at fine resolution. Coe et al. (2008) developed a distributed river model at 5-minute resolution over the Amazon River in which the flood processes are parameterized using information from the 1km resolution Shuttle Radar Topography Mission (SRTM) data set. Such fine resolution information provides physically based fractional flooding inundation of grid cells from a statistical representation of sub-grid-scale floodplain morphology. Over the same basin, Beighley et al. (2009) developed a modelling framework based on a flexible height resolution representation of land surface topography and a fluvial transport system that is capable of providing realistic channel and floodplains hydraulic characteristics on a daily time scale. Fan and Miguez-Macho (2010) proposed a simple hydrologic framework applied over North America at 30-second resolution to simulate the

wetland and inland water bodies based on dynamic and prognostic groundwater water table depth that can support surface water bodies by maintaining a saturated substrate. Nevertheless, only the wetlands distribution and spatial extent was investigated in this study without the evaluation of their time-tendency or dynamic. At a coarse resolution (1° by 1°), Decharme et al. (2008) developed a coupled LSM-RRM flood scheme over South-America to represent the floodplain dynamics and its impact on continental evapotranspiration and energy budget for large scale applications and climate modeling trough the use of a simple sub-grid topographic relationship between water volume and flooded area. At a similar resolution (0.5° by 0.5°), Dadson et al. (2010) proposed also a coupled LSM-RRM flood scheme over the Niger inland delta region based on sub-grid topographic statistics. In terms of model evaluation, the Coe et al. (2008), Decharme et al. (2008) and Dadson et al. (2010) schemes were the first to be evaluated using conjointly satellite-derived inundation estimates and in-situ river discharge observations whereas in previous studies only the impact of the flood processes on river discharges was investigated (Coe 1998; Krinner et al. 2003; Coe et al. 2002; Guntner et al. 2007; Beighley et al. 2009).

Focusing on Decharme et al. (2008), the simple river flood scheme attempts to represent the space-time variations of the large seasonal inundations at continental scale, but excluding lakes, large ponds and wetlands. The flood dynamics is described through the daily coupling between the Interaction Sol-Biosphère-Atmosphère (ISBA) LSM (Noilhan and Planton 1989) and the Total Runoff Integrating Pathways (TRIP) RRM (Oki and Sud 1998) including a prognostic flood reservoir added by Decharme et al. (2008). This reservoir fills when the river height exceeds the river bankfull height and vice-versa. Its dimension evolves dynamically according to the flood water mass and the sub-grid topography in a given grid-cell. The reservoir interacts with the soil hydrology through infiltration and with the overlying

atmosphere through precipitation interception and free water surface evaporation. The evaluation was made in off-line mode over South-America. Results showed that due to a basin-scale increase in surface evaporation, the monthly discharges over the Parana River basin were drastically improved while over the Amazon basin, the improvement on the simulated discharge was mainly related to the introduction of a delay in the timing of river flow through water store in the flooded area. In addition, an acceptable agreement between the simulated flooded areas and satellite-based inundation estimates was also found. These results were similar to that found at finer resolution by Coe et al (2008) over the Amazon.

The main objective of the present study is to evaluate and to assess the robustness of this flood scheme at the global scale, an essential step before its use into coupled continent-atmosphere climate studies. This evaluation is done in off-line mode in which the ISBA-TRIP flood model is forced by the global meteorological data set provided by Princeton University (http://hydrology.princeton.edu) on a 3-hourly time step and at 1° resolution (Sheffield et al. 2006). As proposed by Coe et al. (2008) and Decharme et al. (2008) but only at regional to continental scale, the model outputs are evaluated against in situ river discharge measurements at 122 gauging stations as well as again satellite-derived inundation estimates from Prigent et al. (2007) now available from 1993 to 2004 (Papa et al., 2010a). This original evaluation strategy for a global scale study permits to evaluate both the floodplain climatology and variability, which is an important issue for possible feedbacks on the climate system, and for the impact of flood events on simulated river discharge and water budget. The ISBA-TRIP flood scheme is presented in section 2. The experimental design, the specific parameters of the floodplain parameterization, and the different data sets are described in section 3. Results are shown in section 4 while a discussion and the main conclusions are provided in sections 5 and 6 respectively.

2. The ISBA-TRIP flood model

2.1. Review of ISBA-TRIP

ISBA is a relatively simple LSM that uses the force-restore method to calculate the time evolution of the surface energy and water budgets (Noilhan and Planton 1989). It includes a comprehensive sub-grid hydrology to account for the heterogeneity of precipitation, topography and vegetation in each grid cell. A TOPMODEL approach (Beven and Kirkby, 1979) has been used to simulate a saturated fraction, f_{sat}, where precipitation is entirely converted into surface runoff (Decharme et al. 2006). Infiltration is computed via two sub-grid exponential distributions of rainfall intensity and soil maximum infiltration capacity. Finally, a tile approach is used to represent land cover and soil depth heterogeneities (Decharme and Douville 2006a).

The original TRIP RRM was developed by Oki and Sud (1998) at the University of Tokyo. It was first used at Météo-France to convert the simulated runoff into river discharge using a global river channel network at 1° resolution. In the new ISBA-TRIP CHS (Decharme et al. 2010), TRIP takes into account a simple groundwater reservoir which can be seen as a simple soil-water storage and a variable stream flow velocity as proposed by Arora and Boer (1999). This variable velocity, v (m.s^{-1}), is computed via the Manning's formula:

$$v = \frac{\kappa}{n} R^{2/3} s^{1/2} \qquad (1)$$

where s (m.m^{-1}) is the downstream river height loss per unit length approximated as the river bed slope, R (m) the hydraulic radius, κ (m^{-3}.s^{-1}) a constant equal to 1, and n the dimensionless Manning friction factor which varies from the upstream part to the mouth of each basin (see

section 3). The hydraulic radius is related to the stream water depth, h_s (m), calculated from the stream water mass, S (kg), assuming a rectangular river cross-section (Arora and Boer, 1999):

$$R = \frac{W h_s}{W + 2h_s} \quad \text{where} \quad h_s = \frac{S}{LW\rho_w} \tag{2}$$

where ρ_w (kg.m^{-3}) is the water density, W (m) the bankfull river width, and L (m) the river length that takes into account a meandering ratio of 1.4 as proposed by Oki and Sud (1998). TRIP is then based on two prognostic equations for the stream reservoir and the groundwater reservoir, G (kg):

$$\begin{cases} \dfrac{\partial S}{\partial t} = Q_{in}^{S} + \dfrac{G}{\tau} - \dfrac{v}{L} S \\ \dfrac{\partial G}{\partial t} = Q_{sb} - \dfrac{G}{\tau} \end{cases} \tag{3}$$

where Q_{sb} (kg.s^{-1}) is the deep drainage from ISBA, Q_{in}^{S} (kg.s^{-1}) the sum of the surface runoff from ISBA within the grid cell with the water inflow from the upstream neighboring grid cells, and τ (s) the uniform and constant time delay factor of the groundwater reservoir which is fixed to 30 days. This last reservoir does not represent the groundwater dynamics but only delays the groundwater flow contribution to the surface river reservoir within a particular grid cell: the deep drainage is fed into the surface reservoir with a time delay factor of τ. More details can be found in Decharme et al. (2010).

2.2. The flood scheme

As proposed by Decharme et al. (2008), a simple coupling between ISBA and TRIP is proposed and the floodplains are explicitly represented into the surface water and energy budgets computed by ISBA. A floodplain reservoir, F (kg), is added in TRIP that is now based on three prognostic equations:

183
$$\begin{cases} \dfrac{\partial S}{\partial t} = Q_{in}^{S} + \dfrac{G}{\tau} - \dfrac{v}{L} S - Q_{in}^{F} + Q_{out}^{F} \\ \dfrac{\partial G}{\partial t} = Q_{sb} - \dfrac{G}{\tau} \\ \dfrac{\partial F}{\partial t} = Q_{in}^{F} - Q_{out}^{F} + \left(P_f - I_f - E_f\right) \end{cases} \quad (4)$$

184 where Q_{in}^{F} and Q_{out}^{F} (kg.s^{-1}) represent the flood inflow and outflow respectively, and P_f, I_f and
185 E_f (kg.s^{-1}) the precipitation interception by the floodplains, the re-infiltration and the direct free
186 water surface evaporation estimated by ISBA respectively. I_f occurs if the flooded fraction,
187 f_{flood}, calculated according to the subgrid topography (Appendix A) is superior to the soil
188 saturated fraction, f_{sat}, and depends on the soil maximum infiltration capacity. In other words,
189 the floodplains cannot infiltrate the fraction of the grid-cell for which the soil is saturated. To a
190 first approximation, it allows to simply represent the fact that the actual floodplains evolve
191 according to the presence of shallow aquifer and water table depth variations.

192 As shown in Figure 1a, a simplified rectangular geometry is assumed to represent the
193 cross section between the floodplain and the river reservoirs in each grid cell. River flooding
194 arises when the water height of the stream reservoir is higher than the critical bankfull height,
195 h_c, and the flood outflow and inflow from this reservoir (Equation 4) are given by:

196
$$\begin{cases} Q_{in}^{F} = \dfrac{v_{in}}{W + W_f} M_f \\ Q_{out}^{F} = \dfrac{v_{out}}{W + W_f} min\left(M_f, F\right) \end{cases} \quad (5)$$

197 where W_f (m) is the floodplain width (Appendix A), and M_f (kg) the potential inflow (positive
198 M_f) or outflow (negative M_f) assuming an equilibrium state between the stream and the
199 floodplain water depth:

200
$$M_f = \rho_w L_f W \left(h_s - h_c - h_f\right) \quad (6)$$

where L_f (m) and h_f (m) are the length along the river and the depth of the floodplains, h_s (m) the water height of the stream reservoir, and h_c (m) the critical bankfull river height. $W+W_f$ represents the distance covered by M_f from the stream to the floodplains or conversely. v_{in} and v_{out} (m.s^{-1}) are the flood inflow and outflow velocities computed using the Manning's formula:

$$v_{in,out} = \frac{s_{in,out}^{1/2}}{n_f} R_{in,out}^{2/3} \quad (7)$$

where n_f is the Manning roughness coefficient for the floodplains that varies according to the vegetation type (section 3) while $s_{in,out}$ (m.m^{-1}) and $R_{in,out}$ (m) are the inflow (or outflow) slope and hydraulic radius respectively at the interface between the floodplain and the river stream. More details can be found in Appendix A. Note that over Greenland, variable flow velocity and floodplains are not activated and a constant flow velocity of 0.5 m.s^{-1} is used.

3. **Experimental design**

3.1. TRIP specific parameters

As discussed in Decharme et al. (2010), a special attention has been paid to the computation of the river bed slope at 1° by 1° resolution. River bed slope is indeed a critical parameter to compute velocity via the Manning formula (Equation 1). The STN-30p Digital Elevation Model (DEM) provided at 0.5° by 0.5° resolution by the ISLSCP2 database [http://islscp2.sesda.com] has been used. The STN-30p DEM was heavily edited to represent the actual elevation along the river network on a global scale, based on the aggregated HYDRO1K DEM at 1km resolution. Further adjustments were made to eliminate some of the unrealistic rapid slope changes in the STN-30p DEM along the global river network. As described in Decharme et al. (2010), the STN-30p DEM was finely interpolated at 1° by 1° resolution. To sum up, a 1° grid box is composed by four 0.5° grid boxes. If one of the four

0.5° grid boxes represents a mountain while the three other correspond to the valley where the major river flows, the interpolation to 1° resolution is only made via the averaging of the three valley's 0.5° grid boxes. This approach permits to compute elevation along the river at 1° resolution and to calculate the river bed slopes with a better accuracy.

In this study, the Manning friction factor varies arbitrary from 0.04 near the river mouth to 0.06 in the upstream grid cells. This factor can be defined as "the resistance of the bed of a channel to the flow of water in it". As discussed in Decharme et al (2010), it is difficult to compute at global scale. It generally varies from low values for natural streams with deep pools as the river mouth to higher values for upstream small rivers. Common estimates give values around 0.024-0.075 for natural streams (Barnes 1967). Previous global studies generally used a global constant value of 0.035 (Arora et al. 1999, Arora and Boer 1999, Lucas-Picher et al. 2003), which has strong limitations given that the values greatly vary in natural streams. Here, it is assumed that upstream grid cells represented the narrower rivers and that the mouths could be seen as a "natural stream with deep pools" in each basin. As a consequence, a linear relationship is taken between the Manning *n* and the river stream order, *SO*, given by TRIP in each grid cell of a given basin:

$$n = n_{min} + \left(n_{max} - n_{min}\right)\left(\frac{SO_{max} - SO}{SO_{max} - SO_{min}}\right) \quad (8)$$

where n_{max} and n_{min} are the maximum and the minimum value of the Manning friction factor (respectively equal to 0.06 and 0.04), SO_{min} and SO_{max} the minimum and maximum stream order in each basins of the TRIP network.

The river width is an important parameter because it is jointly used in the simulation of the river flow and the floodplain dynamics. It is computed over the whole TRIP network via an empirical mathematical formulation that generally describes a geomorphologic relationship

between W and the mean annual discharge at each river cross section (Knighton 1998; Arora and Boer 1999; Moody and Troutman 2002):

$$W = max\left(30, \beta \times Q_{yr}^{0.5}\right) \quad (9)$$

where Q_{yr} (m^3/s) is the annual mean discharge in each grid cell estimated using the global runoff database from Cogley (1998). As shown in many studies, the β coefficient can vary drastically from one basin to another (Knighton 1998; Arora and Boer 1999; Moody and Troutman 2002). As for example, using width and discharge observations, Arora et al. (1999) found a value of 32 for the Amazon River while Moody and Troutman (2002) found 17 for the Mississippi River. In this study, β is fixed for five different hydrological regions of the world as shown in Figure 1b. β is 32 for equatorial or sub-tropical basins, 25 for arctic or sub-arctic basins, 20 for "monsoon" basins, 15 for temperate basins, and 13 for semi-arid or arid basins. Each value has been chosen so that the resulting river mouths match the following values: 15000m for the Amazon (equatorial), 2000-3000m for arctic rivers, 500-2000m for temperate rivers, 1500-3000m for monsoon rivers, and less than 1000m for semi-arid or arid rivers. The spatial distribution of the river width is given in Figure 1c while some calculated values are given in Table 1.

As shown in Decharme et al. (2008) over South-America, the key parameter for the floodplain parameterization is h_c, the critical river bankfull height. In this previous study, h_c was computed via a linear relationship with the river width. Nevertheless, this previous formulation induces a drastic sharp transition in h_c value at the basin boundary, especially in the upstream part of the Amazon. In this study, a non linear function is proposed:

$$h_c = W^{1/3} \quad (10)$$

A global distribution of h_c is given in Figure 1d. However, as described in the next section, two additional sensitivity experiments are also done with h_c±25% leading to an increase or a decrease in bankfull height from about 1m to 6m (Table 1).

Finally, the Manning roughness coefficient for the floodplains, n_f, is computed by using the spatial distribution of the 12 vegetation types at 1° resolution specified according to the 1-km ECOCLIMAP data base of Météo-France (Masson et al. 2003). Indeed, the vegetation has generally a non-negligible impact on this roughness coefficient (Thomas and Nisbet 2006) and a simple solution is used:

$$n_f = \sum_{i=1}^{12} \left(vegt_i \times n_i \right) \quad (11)$$

where n_i is the floodplain roughness coefficient corresponding to one vegetation type (Table 2), and $vegt_i$ the grid-cell fraction of each vegetation types. As shown in Figure 2, n_f, is larger in densely vegetated areas and lower for sparser vegetated regions.

3.2. Experiments

The experimental design is similar to Decharme et al. (2008). An off-line hydrological simulation with the flood scheme (*FLD*) is compared to a control experiment without floodplains (*CTL*). In addition, two sensitivity experiments to the h_c parameter are also performed globally using h_c±25%. These two simulations permit to present a sensitivity study to the h_c parameter. In Decharme et al (2008), a comparable sensitivity experiment to h_c over South-America basins had suggested that the model is relatively robust, without any particular tuning, but such conclusion must be investigated and confirmed at global scale. ISBA and TRIP are integrated at 1° resolution using 30-min and 1h time step respectively over 1983-2006 where the first three years are considered as spin-up. Every day, the total runoff (surface

290 runoff + deep drainage) simulated by ISBA is fed into TRIP which returns to ISBA the grid-
291 cell floodplain fraction and the flooded water mass in order to calculate P_f, I_f, E_f (Equation 4)
292 and the surface energy budget.

293 The global meteorological forcing is provided by Princeton University
294 (http://hydrology.princeton.edu) at a 3-hourly time step and 1° resolution. This data set is based
295 on the National Center of Environmental Prediction-National Center for Atmospheric Research
296 (NCEP-NCAR) reanalysis. Sheffield et al. (2006) carried out corrections of the systematic
297 biases in the 6-hourly NCEP-NCAR reanalyses via hybridization with global monthly gridded
298 observations. In addition, the precipitation was disaggregated in both space and time at 1°
299 resolution via statistical downscaling and at 3-hourly time step using information from the 3-
300 hourly Tropical Rainfall Measuring Mission (TRMM) data set. More details about this forcing
301 product can be found in Sheffield et al. (2006). The 3-hourly precipitation from Sheffield et al.
302 (2006) is hybridized to match the monthly value from the Global Precipitation Climatology
303 Center (GPCC) Full Data Product V4 (http://www.dwd.de). As shown by Decharme and
304 Douville (2006b), the GPCC climatology appears to be a better product to perform global
305 hydrological applications.

306 The land surface parameters used by ISBA are specified according to the 1-km
307 resolution ECOCLIMAP database developed at CNRM (Masson et al. 2003). The soil textural
308 properties are given by the Harmonized World Soil Database of the Food and Agricultural
309 Organization at 1 km resolution (FAO 2009). Vegetation parameters are defined using two
310 vegetation data sets: the Corine Land Cover Archive at 250 m resolution over Europe and from
311 the University of Maryland (Hensen et al. 2000) data set elsewhere at 1 km. All topographic
312 information is specified according to the 30-arcsecond resolution GTOPO30 data set
313 (http://eros.usgs.gov/products/elevation/gtopo30/gtopo30.html) and the 1 km resolution

HYDRO1K product (Verdin and Greenlee 1996; http://eros.usgs.gov/#/Find_Data/Product_and_Data_Available/gtopo30/hydro).

3.3. Evaluation data sets

Over the evaluation period (1986-2006), the simulated discharges are compared to gauging measurements from the HyBAm data set (http://www.mpl.ird.fr/hybam/) for the Amazon, the R-ArticNet database (University of New Hampshire; http://www.r-arcticnet.sr.unh.edu/v3.0/index.html) for high latitude basins, the Bangladesh Water Development Board data set for the Ganges as described in Papa et al. (2010b), and elsewhere from the Global Runoff Data Center (GRDC; http://www.grdc.sr.unh.edu/index.html). This evaluation data set combines in total 122 gauging measurements distributed over the globe (Figure 3). Only sub-basins with drainage areas of at least 10^5 km² and with a minimum observed period of four years are kept.

In addition, the satellite-derived inundation estimates are used to evaluate the spatial distribution and the time evolution of the simulated flooded areas over the 1993-2004 period (Prigent et al 2007; Papa et al. 2010a). This data set quantifies at the global scale the monthly variations of the distribution of surface water extent at ~25km sampling intervals. As described in detail by Prigent et al (2001, 2007), it is derived from a complementary suite of satellite observations: Normalized Difference Vegetation Index (NDVI) given by the Advanced Very High Resolution Radiometer (AVHRR); active microwave from the European Remote Sensing (ERS-1) scatterometer backscatter at 5.25 GHz; and finally, passive microwave emissivities between estimated from the Special Sensor Microwave/ Imager (SSM/I) by removing the contributions of the atmosphere (water vapor, clouds, rain) and the modulation by the surface temperature, using ancillary data from visible and infra-red satellite observations from the

337 International Satellite Cloud Climatology Project (ISCCP) and the National Centers for
338 Environmental Prediction (NCEP) reanalysis. Global monthly-mean surface water extent data
339 set is created with a 0.25° spatial resolution at the equator and is currently available from 1993
340 to 2004 (Prigent et al 2007; Papa et al 2010a). In the present study, this data set is then
341 interpolated at 1° resolution and named hereafter *P07*. The global distribution of the *P07* mean
342 inundated areas from 1993 to 2004 is given in Figure 4a.

343 Because P07 does not make distinction between the diverse anthropogenic and/or
344 natural water bodies while the ISBA-TRIP output must be compared with floodplain areas
345 only, two additional data sets are used to hybridize *P07* in order to conserve information on
346 flood interannual variability only: the Global Lakes and Wetland Database (GLWD) and the
347 Monthly Irrigated and Rainfed Crop Areas around the year 2000 (MIRCA2000) database. The
348 GLWD data (Lehner and Döll 2004) gives the global distribution of 12 types of surface water
349 bodies as lakes, wetland and floodplains at 30arc second resolution (~1km at the equator). In
350 this study, this product is interpolated at 1° resolution for lake, reservoir, and bog, fen and mire
351 types as shown in Figure 4b as well as for river, floodplain and flooded forest types as shown
352 in Figure 4c. The MIRCA2000 product (Portmann et al. 2010) provides both irrigated and
353 rainfed crop areas of 26 crop classes for each month of a year around the year 2000 at 5arc
354 minute resolution (~9.2km at the equator). This product, which represents the sum of the 26
355 irrigated crop classes, is also interpolated at a 1° resolution and the global distribution of the
356 annual maximum is given in Figure 4d.

357 Figure 4 shows that *P07* cannot be directly compared with the simulated floodplain
358 extents because it makes no distinction between floodplains and other surface water bodies.
359 P07 is then hybridized with the GLWD and the MIRCA2000 products to build an alternative
360 product more comparable with the model simulations. This hybridization is carried out

following two steps. First, the GLWD lakes, and bogs, fens and mires areas, L_{GLWD}, as well as the MIRCA2000 annual cycle I_{mth}, are subtracted from *P07* where the GLWD rivers, floodplains and intermittent lake/floodplain areas, F_{GLWD}, exist:

$$P_{07/GM}(t) = \delta \times max[0, P07(t) - L_{GLWD} - I_{mth}] \quad \begin{vmatrix} \delta = 1 & \forall F_{GLWD} > 0 \\ \delta = 0 & \forall F_{GLWD} = 0 \end{vmatrix} \qquad (12)$$

where *t* (month) is the time and $P_{07/GM}$ the new final product.

4. **Results**

4.1. Flooded area

Figure 5 shows the comparison between the mean annual cycles of both the $P_{07/GM}$ inundated areas and the simulated *FLD* floodplains. For each season, the global distribution of the floodplains simulated by *FLD* appears robust even if the simulated flooded areas seem to be underestimated especially over South Asia and Northern Canada. The comparison of *FLD* with the two sensitivity experiments ($h_c \pm 25\%$), based on the 1993-2004 mean flooded areas and given in Figure 6, underlines the impact of the river bankfull height on the simulated flooded areas. As expected, a lower h_c induces larger floodplains and inversely. Following Equation 6, if h_c decreases (increases), the potential inflow into the floodplain reservoir increases (decreases) according to Equation 6, and then the resulting flooded areas also increase (decrease). Note that $h_c+25\%$ drastically underestimates $P_{07/GM}$ globally while $h_c-25\%$ is in better agreement except over Europe and Russia where the flooded areas appear too dense.

Figure 7 shows the basin-averaged annual cycles of monthly floodplain fractions. Over the Arctic basins (Mackenzie, Ob, Lena), the main difference between *P07* and $P_{07/GM}$ is linked to the important density of lakes, especially over the Mackenzie basin, and bogs, fens and

mires elsewhere (Figure 4b). The flooded areas are smaller over East Siberia (Lena) than over the Ob and/or Mackenzie basins, and generally located near the river stream (Figure 6a). At these high latitudes, according to Figure 5, the *FLD* simulated flooded area seems to be underestimated, especially during summer (June-July-August). In addition, the simulated flooded area starts earlier than the satellite-derived estimates. Over Central and/or Eastern Europe basins, the main difference between *P07* and $P_{07/GM}$ is linked to the presence of lakes and reservoirs over the Volga basin and irrigation over the Danube. Over the Volga basin, the *FLD* simulated flooded areas are overestimated during spring but the mean annual cycle is in agreement with satellite-based estimates. The same behaviour is observed over the Danube with larger differences but still in the $P07/P_{07/GM}$ estimated range. Over North America (Mississippi), the main $P07/P_{07/GM}$ difference is due to irrigation and the Mississippi simulated flooded fractions are relatively consistent with $P_{07/GM}$. Over Africa (Congo, Niger), a small fraction of lakes explains the $P07/P_{07/GM}$ difference. The Congo basin exhibits small floodplain areas and *FLD* is slightly underestimated. Over the Niger, while the amplitude of the simulated annual cycle appears acceptable, the *FLD* flooded areas start later and shows a too long persistence of the flooding season. Over South America (Amazon, Parana), the small $P07/P_{07/GM}$ difference is linked to the presence of lakes. The *FLD* simulated floodplains are generally underestimated. Over South Asia (Ganges, Mekong), the $P07/P_{07/GM}$ difference is mainly due to intensive irrigation. The *FLD* simulated floodplains are poorly reproduced with a clear underestimation and a flooded season that starts too late (~2-3 months later). Some explanations will be given in the discussion section. Regarding the sensitivity of h_c, the difference between *FLD* and $h_c \pm 25\%$ appears non-negligible everywhere. According to Figure 6 and despite the general poor results over South Asia, $h_c + 25\%$ accentuates the *FLD* underestimation while $h_c - 25\%$ attempts to generally overestimate the simulated flooded areas

except over the Mackenzie, the Mississippi, the Congo and the Parana where the simulated annual cycles seem to be better reproduced.

Moving to inter-annual variability, Figure 8 shows the basin-averaged anomalies of the floodplain extent for $P_{07/GM}$, *FLD* and $h_c \pm 25\%$. The correlation and Root Mean Square Error (RMSE) for each experiment are also given. Generally speaking, the monthly anomalies are reasonably reproduced by *FLD*, especially over the Ob, Mississippi, Congo, Niger, Parana and Mekong basins even if these results cannot be considered satisfactory due to some poor correlation scores. The simulated flooded areas are smoothed when h_c increases ($h_c+25\%$) and then the RMSE scores are generally improved to the detriment of the monthly correlations. The main exception is observed over Siberia (Ob, Lena) where all scores are improved. Conversely, a decrease in h_c ($h_c-25\%$) increases the signal variability and then favors the correlations to the detriment of RMSE scores. Nevertheless, over all basins the sensitivity of h_c remains generally relatively weak compared to the model error.

4.2. River discharges

It is now well known that seasonal flooding affects the river flow in many regions of the world from tropical to high latitude basins. Without the parameterization of flooding and their variations, CHSs tend to drastically overestimate Tropical and/or West African river discharges, which can be mainly related to the non representation of direct evaporation from free surface water bodies (Ngo-Duc et al. 2005; Decharme and Douville 2007, Decharme et al. 2008, Alkama et al. 2010). Over Arctic basins and especially the Ob and Mackenzie Rivers, large floods occur in May/June when the mass of water in the river increases due to snow melting. Consequently, a significant part of the water is not available for flowing and flooding limits the stream flow velocity compared to basins with more negligible floodplain processes

(Yenisey, Lena). For example, over the Ob, large floods appear after the snowmelt period and can cover an important part of the basin, especially at the confluence of the Ob and the Irtysh (Figure 5 and 7). The observed flow velocity is generally limited to 0.5 $m.s^{-1}$ due to the significant amount of water stored in these large floodplains (Kouraev at al. 2004, Frappart et al. 2010) whereas without flooding, this velocity can be drastically faster and can reach 1 $m.s^{-1}$ to 2 $m.s^{-1}$ (Arora and Boer 1999, Decharme et al. 2010). Such processes that delay and attenuate the peak discharge during large floodplain storage are also dominant over the Amazon basin (Coe 2008, Decharme et al. 2008).

In this section, the simulated river discharges with (*FLD*) and without (*CTL*) flooding are now compared to gauging measurements. The present evaluation stage is important for hydrological applications as well as for future climate studies. Beside the direct evaluation of the simulated discharge scores, it permits to assess the interaction between the floodplains and the river flow as well as to evaluate indirectly the ISBA-TRIP water budget. This evaluation is done with the help of the most popular skill scores used in hydrology. These scores are: the annual discharge ratio criterion ($Ratio = \overline{Q_{sim}} / \overline{Q_{obs}}$), the RMSE, and the efficiency (*Eff*) (Nash and Sutcliffe, 1970) criterion that measures the model ability to capture the monthly discharge dynamics. This last skill score is defined as follows:

$$Eff = 1.0 - \frac{\sum \left(Q_{sim}(t) - Q_{obs}(t)\right)^2}{\sum \left(Q_{obs}(t) - \overline{Q_{obs}}\right)^2} \qquad (13)$$

where $\overline{Q_{obs}}$ represents the observed temporal mean. *Eff* can be negative if the simulated discharge is very poor and is above 0.5 for a reasonable simulation.

Figure 9 shows the global distribution of the difference between the *CTL* and *FLD* discharges in terms of annual ratio, efficiency, and monthly anomaly RMSE. The annual ratio

is reduced (*FLD-CTL ratio* difference inferior to -0.05 in Figure 9b) over 35% of the 122 gauging stations and mainly where this annual ratio is superior to 1.3 (25% of all stations). As it will be shown later, this decrease in annual discharge is related to the increase in continental evapo-transpiration via the direct evaporation of the floodplains. The efficiency scores are increased (*Eff* difference superior to 0.05 in Figure 9d) over 50% of all stations and only reduced (*Eff* difference inferior to -0.05) for 5 stations. The monthly anomaly RMSE scores are also improved (RMSE difference inferior to -0.01 in Figure 9f) over 50% of all stations and only deteriorated (RMSE difference superior to 0.01) for 4 stations. In other words, *FLD* reduces the annual ratio especially over the stations where the *CTL* discharge overestimations are the largest (Figure 9a). This fact is particularly relevant over Africa, Australia, and South America. As discussed before, over these regions this decrease in simulating river discharges is mainly responsible to the general positive impact on both the efficiency scores (Figure 9d) and the monthly anomalies RMSE (Figure 9f). Elsewhere, when an improvement is found, it is mainly due to a weaker peak in the river flow related to the floodplain storage. Conversely, some score deteriorations appear over Eastern Siberia (Lena, Amur) and near the mouth of the Mississippi River where the flooded areas are the largest (Figure 6a and b). As shown in Figure 9a, the Lena (or Amur) River discharges are clearly underestimated by *CTL*. So, even if *FLD* induces a slight decrease in river discharges, this decrease is sufficient to impact the efficiency scores. Over the Mississippi, the simulated floodplains seem to be too important at least near the downstream part of the basin.

As shown in Figure 10 which represents the global distribution of the h_c sensitivity on the simulated river discharges in terms of efficiency and monthly anomalies RMSE, an increase in h_c and then a decrease in simulated flooded areas (Figure 5c) improve these skill scores (+0.15 for *Eff* and -0.02 for RMSE) near the mouth of the Mississippi basin (Figures 10a

and 10c). Conversely, a decrease in h_c and then an increase in simulated flooded areas (Figure 5d) attempt to improve the scores over many regions of the globe. Exceptions are found over Siberia, the Amazon, South Europe, a part of South Asia and accordingly the downstream part of the Mississippi basin. The efficiency scores are increased (h_c*-25%-FLD Eff* difference superior to 0.05 in Figure 10b) over 45% of all stations and only reduced (*Eff* difference inferior to -0.05) over 15%. The monthly anomaly RMSE scores are also improved (RMSE difference inferior to -0.01 in Figure 10d) over 30% of all stations and only deteriorated (RMSE difference superior to 0.01) over 10%. These results underline the non-negligible impact of the h_c value on the quality of the simulated discharges.

Focusing on the downstream station of the major world river basins, Figure 11 compares the mean annual cycle of the simulated and observed discharges. The skill scores given on each plot are calculated over the actual signal and the entire period, and not over the annual cycle. The comparison between *FLD* and *CTL* confirms the general improvement of the simulated discharges pointed out by Figure 9 with the use of the flood scheme. Over the Volga, the Danube, the Parana, the Niger and, to a lesser extent, the Congo River basin, this improvement is mainly related to a decrease in annual discharge ratio. This process is also relevant over the Mackenzie, the Ob or the Amazon basins but the improvement is mainly due to a better simulation of the river flow peak as already discussed. Exceptions are found over the Lena and the Mississippi, and to a lesser extent over the Ganges and the Mekong basins. Over the Lena, as already said, the simulated streamflow is clearly underestimated and a slight decrease in river discharges (due to simulated floodplains) is sufficient to impact the skill scores independently of the value of h_c. However, over the Lena, the Ganges and the Mekong basins the *FLD* simulation remains acceptable with regards to the *CTL* model errors. For example over the Ganges basin, while the annual peak of discharge is more consistent in *FLD*

than in *CTL*, *FLD* conserves the general weakness found in *CTL* where the high discharge season starts later and remains longer than in the observed discharges. This result is in agreement with the same drawback found in simulated floodplain extent (Figure 7). The good scores given by the h_c+25% simulation compared to the others over the Mississippi basin confirm that the simulated flooded areas are too large near its downstream part. Finally, Figure 11 confirms that a decrease in h_c and then an increase in simulated flooded areas can improve the quality of the simulated discharges over many rivers of the globe. Over non-improved basins (Siberian rivers, Danube, Mississippi, Amazon and Ganges), the decrease in h_c induces too large floodplains and then smoother and unrealistic simulated annual cycle.

Moving to the discharge inter-annual variability, Figure 12 shows the comparison between the simulated and observed discharges over the same gauging stations than in Figure 11. The RMSE and correlation of each simulation are also given. In general, *FLD* improves these scores and then the simulated inter-annual variability, which confirms results given in Figure 9f. The main impacts are found over the Arctic basins (Ob, Mackenzie), South America (Amazon, Parana) and West Africa (Niger) even if the correlation is reduced. No significant change is observed over the Danube and South Asian basins, and except over the Mississippi basin, a slight improvement is found elsewhere. Regarding the sensitivity of h_c, beside some exceptions (Ob, Mississippi, Parana, Ganges) where one of the three floodplain simulations is clearly better than the others, the monthly discharges anomalies are generally not impacted by the value of h_c.

4.3. Water budget

The implementation of the flood scheme leads to a clear reduction in the simulated river discharges (from 5% to 20% compared to *CTL*) over some large river basins (Ob, Mackenzie,

Volga, Mississippi, Parana, Niger, and Ganges), while others remain relatively unchanged (less than 5% compared to *CTL*). This reduction in river discharges is logically balanced by an increase in evapo-transpiration. Figure 13 compares the mean annual cycle of the *FLD* simulated evapo-transpiration with *CTL*. The global surface evaporation increase is around 2% and is especially important during spring (March, April, and May). Despite the fact that this increase can appear negligible in some cases, it can also be very important over some regions (North Canada, East Europe, West Siberia, South America or South Africa) as shown in Figure 13. Regarding the sensitivity of h_c, the global surface evaporation increase is around 1% for h_c*+25%* and 4% for h_c*-25%*, and it is also more important during spring. The fact that a decrease in h_c induces a strong increase in evaporation is linked to the overestimation of the simulated flooded areas over West Siberia and Europe with h_c*-25%* (Figure 6d). With regards to these global values, the sensitivity of h_c is also non-negligible on the land surface water budget.

5. **Discussion**

The results suggest that the proposed simple flood scheme generally provides a reasonable estimation of the spatio-temporal variability of the flooded areas. In addition, it improves the simulated river discharge over 50% of the 122 gauging stations while it deteriorates the skill score over only 4% of the cases. Elsewhere, the flood scheme has logically no impact because flood processes do not take place over all basins of the world. However, it must be recognized that the basin-scale comparison with satellite-derived flooded area estimates is not very impressive. As pointed out in the introduction, this study is the first attempt to evaluate a simple global two-way flood scheme developed at a coarse resolution where the flood process affects both the surface hydrology (floodplains and river flow) and the

546 continental water and energy budgets. Such global work represents another step toward the
547 physical representation of all inland water bodies in climate models. It is interesting to note
548 that the results of Coe et al. (2008) over the Amazon basin, calculated with a finer resolution
549 model, are coherent with this study and confirm the difficulties to accurately simulate together
550 the floodplains and the discharge dynamics.

551 Some deficiencies appear throughout this evaluation. The simulated floodplains are
552 generally underestimated and over some basins (Africa, South-Asia, Pantanal) the discharges
553 remain drastically overestimated. It can be partially due to uncertainties in the precipitation
554 forcing with regards to the small density of GPCC rain gauges in these regions (Decharme and
555 Douville 2006b). Other causes can be related to some important processes not represented in
556 ISBA-TRIP. The man-made irrigation (especially over South Asia) and/or dams can alter the
557 river flow and increase the continental evapo-transpiration (Sacks et al. 2009). Deep and large
558 aquifers relatively uncoupled to the river over arid or semi-arid basins, such as the Niger,
559 contribute to limit the drainage inflow to the river (Leduc et al. 1997 and 2001). Conversely,
560 shallow aquifers support and feed surface water bodies when the water table depth reaches the
561 surface (Fan and Miguez-Macho 2010). In ISBA, the water table depth evolution is simply
562 parameterized thought a TOPMODEL approach. In TRIP, the deep reservoir does not represent
563 the groundwater dynamics but only delays the groundwater flow contribution to the surface
564 river reservoir within a particular grid cell. As a consequence, dynamical aquifer processes are
565 not represented in this study. This fact may partly explain the general underestimation of the
566 simulated floodplains.

567 Over the West Siberian basins, the well known precipitation bias in the GPCC data
568 (Decharme and Douville 2006b) induces a general underestimation of both simulated flooded
569 areas and discharges that does not permit to evaluate the scheme correctly. However, such

underestimation could be also attributable to the presence of deep permafrost not represented in ISBA in which only the superficial soil ice (from 20 to 35 cm depth) related to the maximum penetration depth of the thermal diurnal wave (Bonne et al. 2000) is parameterized. The permafrost prevents deep drainage and favors the formation of surface water bodies (wetlands, lakes…). This accumulation of surface water can also contribute to feed the floodplains (Kouraev at al. 2004; Price et al. 2005). In addition, all simulations over the Arctic basins show that the simulated flood starts earlier than the satellite-derived ones (Figure 7). Over these regions, the floodplains and river discharges are fed mainly by the springtime snowmelt (Papa et al. 2007, 2008). Considering that the simulated and observed discharges are in phase (Figure 11), the fact that the floodplains appear earlier in ISBA-TRIP is likely not due to an earliness of the snowmelt timing simulated by ISBA. As shown by Alkama et al. (2010) with the same configuration of the ISBA-TRIP model and the same atmospheric forcing than in the present study, the simulated snowmelt timing was well reproduced when compared to the National Snow and Ice Data Center (NSIDC; http://nsidc.org/) data. However, in these regions, P07 results might be questionable. Because the microwave measurements are sensitive to the snow cover, a snow and ice mask based on the same NSIDC data is applied over the Northern Hemisphere to avoid confusion between snow cover and snow-free pixels (Papa et al. 2007 and 2008). An overestimated snow mask might impact the satellite-derived estimates and could be the cause of this slight difference.

The main model deficiencies appear over South Asia (Ganges, Mekong) where the simulated floodplains are drastically underestimated even compared to $P_{07/GM}$ in which the significant irrigated areas have been removed to *P07*. This rice irrigation is intensive after the monsoon season, from the end of September to December (Sacks et al. 2009; Portmann et al. 2010). Consequently, the fact that $P_{07/GM}$ shows important inundated areas throughout the year

is relatively surprising, especially over the Indochina peninsula (Mekong) and at the confluence of the Ganges-Brahmaputra rivers: in these regions, the multi-satellite method might encounter some difficulties in accurately discriminating between very saturated moist soil and standing open water and might overestimate the actual fraction of inundation (Papa et al., 2010a). In addition, hydrological processes in Bangladesh are complicated by the large delta at the confluence of the Ganges and Brahamaputra rivers, which is well captured by satellite (Figure 4a, c and 6a), but not represented by the model. Conversely, the simulated discharges are clearly overestimated after the monsoon season (October to December). This weakness is not due to the flood scheme because the control experiment exhibits the same behavior. It might be rather linked to the intensive rice irrigation that induces large water pumping from the river or aquifers during this period (Sacks et al. 2009; Rodell et al. 2009; Portmann et al. 2010).

Conversely to Decharme et al. (2008), the experiments with different values of the river bankfull height reveal that the sensitivity of the model is not negligible over many regions of the globe. Note however that the h_c range ($\pm 25\%$) chosen in this study is larger than in Decharme et al. (2008). To sum up, the river bankfull height impacts the land surface evaporation, at least at regional scale, and the range of the increase in evaporation due to the presence of flooded area can be more or less intensive according to the h_c values. An increase in h_c induces a decrease in simulated flooded areas that is not robust compared to the satellite-based estimates and globally deteriorates the simulated river discharge scores compared to *FLD*. The main exception appears over the downstream part of the Mississippi basin where an increase in h_c allows better results. Conversely, a decrease in h_c, which induces an increase in simulated flooded areas, is more robust compared to the satellite-based estimates and discharge measurement. Compared to *FLD*, the efficiency scores are improved over 45% of all stations

and only reduced over 15%. This improvement in river discharges score is found especially over North America (excluding the downstream part of the Mississippi basin), South America (excluding the Amazon basin), Africa, Australia, and some basins over Eastern Europe (e.g. Volga) and South Asia (Figure 10b and d). In other words, while h_c could be increased over the Mississippi basin, it also could be decreased over these other regions to improve the model simulations.

This tuning should be based mainly on the river discharge scores, given the large distribution of river gauging measurements over the globe available today, while ensuring a reasonable simulation of the flooded areas compared to the satellite-based estimates. For global hydrological applications such a tuning is certainly not advisable because it should be done with an accurate atmospheric forcing (especially precipitation) which is generally not the case at the global scale. It also could hide some model deficiencies related to the non-representation of irrigation, groundwater dynamics, lakes, large ponds, and wetlands. However for climate studies and from a pragmatic point of view, this tuning could permit to represent the floodplains and especially its related direct evaporation with a reasonable accuracy while the spatio-temporal variations in precipitation are generally poorly represented.

6. **Conclusions**

This study describes the evaluation of the ISBA-TRIP flood model that will be used for global hydrological and climate applications. It is evaluated over the globe using off-line simulations at a 1° by 1° resolution driven by the 1986-2006 3-hourly atmospheric forcing from Princeton University. The flood scheme accounts explicitly for the precipitation interception by the floodplains, the direct evaporation from the free water surface and the possible re-infiltration into the soil. The simulated river discharges are evaluated against 122 in

situ gauging measurements distributed all over the globe, while the simulated flooded areas are compared to satellite-derived inundation estimates from Prigent et al. (2007) and an alternative product using jointly the GLWD database of lakes, wetlands and floodplains (Lehner and Döll 2004) and the MIRCA2000 crop irrigation product (Portman et al. 2010).

The results suggest that the proposed simple flood scheme generally provides a reasonable estimation of the spatio-temporal variability of flooded areas. In addition, the simulated river discharges are improved by this scheme for the majority of the gauging stations affected by floods. This positive impact is mainly related to: (1) an increase in evapo-transpiration and then a decrease in river discharges especially relevant over the regions where the simulated river discharges are overestimated without the flooding scheme; (2) the flood scheme delay and attenuated river peak flow when the floodplain storage is significant. As far as the annual mean water budget is concerned, this increase in evapotranspiration is particularly important at a regional scale and is expected to have a significant regional impact on global climate simulation.

Nevertheless, some deficiencies appear throughout the model evaluation. Different reasons can account for such residual biases: uncertainties in the atmospheric forcing (Chapelon et al. 2002; Fekete et al. 2003, Ngo-Duc et al. 2005; Decharme and Douville 2006b), possible anthropogenic influence on the observed discharges, and deficiencies in the ISBA-TRIP model. Further improvements could be made by adding an explicit representation of irrigation, lakes, marshes, and large ponds. Over high latitudes, the explicit simulation of the permafrost could potentially improve the present results. In addition, the treatment of groundwater in TRIP could be considerably improved by using a two dimensional approach where the water flux between the groundwater and ISBA or the stream reservoir as well as the water exchange between each neighboring grid-cell could be explicitly calculated (Fan et al.

665 2007; Miguez-Macho et al. 2007). In addition, satellite-derived inundation estimates could also
666 show some limitation as for example over South Asia, which exhibits very large inundation
667 extents throughout the year.

668 Besides these reasons, some aspects of the scheme are obviously questionable, such as
669 the empirical computation of the river width, the choice of the river bankfull height, the simple
670 computation of the river slope, the simplified geometry of the river stream and flood reservoirs,
671 or the use of the Manning's formula for computing the mass transfer between them. It must be
672 recognized that the most important parameter is the river width because it mainly controls the
673 good simulation of the river height and the river stream flow velocity (Equations 1 and 2).
674 With the river bankfull depth, it controls also the potential mass of water that can be flooded
675 (Equation 6). The accurate computation of the river slope and/or the value of the Manning's n
676 coefficient are secondary but could help to refine the ISBA-TRIP simulations. The choice of
677 these parameters in this study appear reasonable for this scheme that has been developed for
678 global climate applications, at a relatively low horizontal resolution (0.5° to 1° resolution), and
679 that must be as robust as possible to be applicable over all regions of the world. This first
680 attempt represents another step toward the representation of all inland water bodies in climate
681 simulations. Other limitations are the resolutions of the Digital Elevation Model (DEM) that
682 can induce an underestimation of the simulated flooded fraction through a failure to represent
683 very flat regions or areas smaller than the horizontal and vertical resolution of the DEM (Coe
684 1998, Coe et al. 2008).

685 Finally, the sensitivity experiments reveal the non-negligible impact of the river
686 bankfull height on the quality of the simulated flooded areas and river discharges. It also
687 impacts the intensity of the land surface evaporation increase. These results underline that the

river bankfull height is potentially tunable region by region. However, such a tuning must be taken with caution on the global scale for at least two reasons:

(1) it might be sensitive to the experimental conditions and especially to the quality of the prescribed atmospheric forcing which is less robust than at a regional scale;

(2) it could mask the model deficiencies related to the non-representation of irrigation, groundwater dynamics, lakes, large ponds, and wetlands.

Another way could be suggested: the development of a global database describing the major river characteristics as the stream width and the river bankfull height. Such a database would be an important progress for future hydrological developments.

APPENDIX A: The floodplain dynamics

The flood inflow and outflow velocities computed using the Manning's formula (Equation 7) requires the hydrological slope between the floodplain and the river stream:

$$\begin{cases} s_{in} = \dfrac{max(0, h_s - h_c - h_f)}{(W + W_f)/2} \\ s_{out} = \dfrac{max(0, h_f + h_c - h_s)}{(W + W_f)/2} \end{cases} \quad \text{(A1)}$$

They also require the hydraulic radius assumed rectangular and calculated as follows:

$$\begin{cases} R_{in} = \dfrac{L_f \times max(0, h_s - h_c)}{L_f + 2 \times max(0, h_s - h_c)} \\ R_{out} = \dfrac{L_f h_f}{L_f + 2h_f} \end{cases} \quad \text{(A2)}$$

where W_f (m), L_f (m) and h_f (m) are the width, the length and the depth of the floodplains, h_s (m) the water height of the stream reservoir, h_c (m) the critical height of the river bed, and W (m) the stream river width.

h_f is calculated in each grid-cell with the help of the actual distribution of the local height, h_i (m), determined at a 1 km by 1 km resolution. The assumption is that each pixel, i, represents a sub-basin into a given grid-cell that can be potentially flooded as shown in Figure 14a. Each sub-basin has a triangular form and is associated with a fraction, f_i, of the grid cell area, A. h_i is computed using the local slope, σ_i (°), and flow direction data given by the HYDRO1K data set (Verdin and Greenlee 1996) at 1km resolution:

$$h_i = l\sqrt{\alpha_i}\, tan\left(\sigma_i \frac{\pi}{180}\right) \quad \text{(A3)}$$

where l (m) is the characteristic length of one pixel equal to 1000 m, and α_i is equal to 1 if the local flow direction is north, south, east, or west, and to 2 elsewhere. Therefore, for each h_i a potential mass of flood, $V(h_i)$ (kg), can be simply calculated using a discrete equation:

$$V(h_i) = \rho_w \sum_{0}^{i} V_i \quad \text{where} \quad V_i = \frac{A f_i h_i}{2} \tag{A4}$$

As shown in Figure 14b, the sub-grid distributions of the flooded fraction and the flood depth allow to determine f_{flood}, and h_f at each time step and in each grid-cell via the comparison between the water mass into the floodplain reservoir, F, computed by TRIP (Equation 4) and the sub-grid distribution of this potential mass $V(h_i)$:

$$F = V(h_i) \Rightarrow \begin{cases} f_{flood} = \sum_{0}^{i} f_i \\ h_f = h_i \end{cases} \tag{A5}$$

When f_{flood} is known within the grid cell, W_f and L_f are simply calculated as follow:

$$\begin{cases} L_f = max\left(0.001, r\sqrt{f_{flood} A}\right) \\ W_f = \dfrac{A f_{flood}}{L_f} \end{cases} \tag{A6}$$

where r is the meandering ratio fixed to 1.4 as recommended by Oki and Sud (1998).

Finally, because ISBA uses a single surface temperature, a new fraction, p_{ff}, is added in each grid cell to account for the effect of the floodplains on the surface energy budget. A fraction of vegetation masked by the floodplains, $p_{f,veg}$, is estimated and combined with the TRIP flooded fraction, f_{flood}, as follows to limits the floodplain evaporation under dense canopy:

$$\begin{cases} p_{f,veg} = f_{flood} \times min\left[1, \dfrac{3}{LAI}\right] \\ p_{ff} = (1 - veg) f_{flood} + veg \; p_{f,veg} \end{cases} \tag{A7}$$

where *LAI* (m.m^{-1}) is the leaf area index given by the ECOCLIMAP data base and *veg* the dimensionless fraction of the vegetation in each grid cell. According to the ECOCLIMAP database, the LAI is generally inferior to 3 for low vegetation (e.g., grassland, crops) and superior for high vegetation (e.g., trees, forests). Then, the direct evaporation (or sublimation if the surface temperature is inferior to 0°C), E_f (Kg.m^{-2}), from this flooded fraction is simply estimated by:

$$E_f = p_{ff} \rho_a C_H V_a [q_{sat}(T_s) - q_a] \quad \text{(A8)}$$

where ρ_a (kg.m^{-3}) is the air density, q_a (kg.kg^{-1}) the air humidity, V_a the wind speed (m.s^{-1}), C_H the dimensionless drag coefficient depending upon the thermal stability of the atmosphere and q_{sat} (kg.kg^{-1}) the saturated specific humidity at the surface that depends on surface temperature, T_s (K).

Acknowledgments

This work is supported by the program IMPACT-BOREAL of the French “Agence Nationale pour la Recherche” (ANR), the CYMENT project of the RTRA STAE Toulouse, the “Centre National de Recherches Météorologiques” (CNRM) of Météo-France, and the “Centre National de la Recherche Scientifique” (CNRS) of the French research ministry. The authors would like to thank Christine Delire (CNRS/CNRM) as well as anonymous reviewers for their useful comments on this study.

REFERENCES

Alkama, M. R., M. Kageyama, G. Ramstein, O. Marti, P. Ribstein, and D. Swingedouw (2008) Impact of a realistic river routing in coupled ocean-atmosphere simulations of the Last Glacial Maximum climate. Climate Dynamics, 30, 855–869.

Alkama R., B. Decharme, E. Douville, M. Becker, A. Cazenave, J. Sheffield, A. Voldoire, S. Titeca, P. Lemoigne, 2009: Global evaluation of the ISBA-TRIP continental hydrological system. Part 1: A twofold constraint using GRACE Terrestrial Water Storage estimates and in-situ river discharges. *J. Hydrometeorology*, 11, 583-600.

Alsdorf, D. E., E. Rodrıguez, and D. P. Lettenmaier (2007), Measuring surface water from space, Rev. Geophys., 45, RG2002, doi:10.1029/2006RG000197.

Arora, V.K., and G. J. Boer (1998), A variable velocity flow routing algorithm for GCMs, J. Geophy. Res., 104, 30965-30979.

Arora, V.K., F.H.S. Chiew, and R.B. Grayson (1999) A river flow routing scheme for general circulation models. *J. Geophy. Res.*, 104, 14 347-14 357.

Barnes, H. H., Jr. (1967) Roughness characteristics of natural channels. U.S. Geological Survey Water-Supply Paper 1849, 213p.

Beighley, R. E., K. G. Eggert, T. Dunne, Y. He, V. Gummadi and K. L. Verdin (2009), Simulating hydrologic and hydraulic processes throughout the Amazon River Basin, Hydrological Processes, 23, 1221-1235 (2009), DOI: 10.1002/hyp.7252

Beven, K. J., and M. J. Kirkby, 1979, A physically-based variable contributing area model of basin hydrology, Hydrol. Sci. Bull., 24, 43-69.

770 Boone, A., V. Masson, T. Meyers, and J. Noilhan (2000) The influence of the inclusion of soil
771 freezing on simulation by a soil-atmosphere-transfer scheme. *J. Appl. Meteor.*, 9, 1544-
772 1569.
773 Bousquet, P., P. Ciais, J.B. Miller, E.J. Dlugokencky, D.A. Hauglustaine, C. Prigent, G.R. Van
774 der Werf, P. Peylin, E.G. Brunke, C. Carouge, R.L. Langenfelds, J Lathière, F. Papa, M.
775 Ramonet, M. Schmidt, L.P. Steele, S.C. Tyler, and J. White (2006), Contribution of
776 anthropogenic and natural sources to atmospheric methane variability, Nature, 443, 439-
777 443, doi:10.1038/nature05132.
778 Chapelon N, H. Douville, P. Kosuth, T. Oki (2002), Off-line simulation of the Amazon water
779 balance : a sensitivity study with implications for GSWP, Climate Dyn, 19, 141-154.
780 Coe, M. (1998), A linked global model of terrestrial processes: Simulation of modern rivers,
781 lakes and wetlands, J. Geophys. Res., 103, 8885– 8899.
782 Coe, M. T., M. H. Costa, A. Botta, and C. Birkett (2002), Long-term simulation of discharge
783 and floods in the Amazon basin, J. Geophys. Res., 107(D20), 8044,
784 doi:10.1029/2001JD000740.
785 Coe, M. T., M. H. Costa, and E. A. Howard (2008), Simulating the surface waters of the
786 Amazon River basin: impact of new river geomorphic and flow parameterizations, Hydrol.
787 Proc., 22, 2542-2553, doi:10.1002/hyp.6850.
788 Cogley, J. G. (1979), The albedo of water as a function of latitude, Mon. Wea. Rev., 107, 775-
789 781.
790 Dadson S. J., I. Ashpole, P. Harris, H. N. Davies, D. B. Clark, E. Blyth, and C. M. Taylor
791 (2010), Wetland inundation dynamics in a model of land surface climate: Evaluation in the
792 Niger inland delta region. J. Geophys. Res., 115, D23114, doi: 10.1029/2010JD014474

Decharme B., and H. Douville (2006a) Introduction of a sub-grid hydrology in the ISBA land surface model. Climate Dyn., 26, 65–78.

Decharme B., and H. Douville (2006b) Uncertainties in the GSWP-2 precipitation forcing and their impacts on regional and global hydrological simulations. Climate Dyn., 27, 695–713.

Decharme, B., and H. Douville, 2007: Global validation of the ISBA Sub-Grid Hydrology. *Clim. Dyn.*, **29**, 21 – 37, doi:10.1007/s00382-006-0216-7.

Decharme B., H. Douville, A. Boone, F. Habets, J. Noilhan, 2006: Impact of an Exponential Profile of Saturated Hydraulic Conductivity within the ISBA LSM: Simulations over the Rhône Basin. J. of Hydromet. 7, 61-80.

Decharme, B., H. Douville, C. Prigent, F. Papa, and F. Aires (2008) A niew river flooding scheme for global climate applications : Off-line evaluation over South America. J. Geophys. Res., 113, D11110,doi:10.1029/2007JD009376.

Decharme, B., R. Alkama, E. Douville, M. Becker, A. Cazenave (2010) Global evaluation of the ISBA-TRIP continental hydrologic system. Part 2: Uncertainties in river routing simulation related to flow velocity and groundwater storage. J. Hydrometeorology, 11, 601-617.

Dirmeyer P. A. (2000) Using a global soil wetness data set to improve seasonal climate simulation. J. Climate, 13, 2900–2922.

Dirmeyer P. A. (2001) Climate drift in a coupled land–atmosphere model. J. Hydrometeor., 2, 89–100.

Douville H. (2003) Assessing the influence of soil moisture on seasonal climate variability with AGCMs. Journal of Hydrometeorology, 4, 1044-1066.

Douville H. (2004) Relevance of soil moisture for seasonal atmospheric predictions: Is it an initial value problem? Climate Dyn., 22, 429–446.

817 Douville, H., P. Viterbo, J.F. Mahfouf, and A.C.M. Beljaars (2000a) Validation of the
818 optimum interpolation technique for sequential for soil moisture analysis using Fife data.
819 Monthly Weather Review, 128, 1733-1756.
820 Douville, H., S. Planton., J.F. Royer , D.B. Stephenson, S. Tyteca, L. Kergoat, S. Lafont, and
821 R.A. Betts (2000b) importance of vegetation feedbacks in doubled-CO2 climate
822 experiments. Journal of Geophysical Research,105, n° D11, 14841-14861.
823 Durand F., F. Papa, A. Rahman and S. K. Bala (2010) Impact of Ganges-Brahmaputra
824 interannual discharge variations on Bay of Bengal salinity and temperature during the 1992–
825 99 period, Journal of Earth System Science, revised.
826 Ducharne, A., Golaz, C., Leblois, E., Laval, K., Polcher, J., Ledoux, E., and de Marsily, G
827 (2003) Development of a high resolution runoff routing model: calibration and application
828 to assess runoff from the LMD GCM, J. Hydrol., 280, 207–228.
829 Fan Y., and G. Miguez-Macho (2010) A simple hydrologic framework for simulating wetland
830 in climate and earth system models, Climat. Dyn., DOI: 10.1007/s00382-010-0829-8, On-
831 line First.
832 Fan, Y., G. Miguez-Macho, C.-P. Weaver, R. Walko, et A. Robock, 2007: Incorporing water
833 table dynamics in climate modeling: 1. Water table observations and equilibrium water table
834 simulations. *J. Geophys. Res.*, **112**, D10125, doi: 10.1029/2006JD008111.
835 FAO/IIASA/ISRIC/ISSCAS/JRC (2009) Harmonized World Soil Database (Version 1.1).
836 FAO, Rome, Italy and IIASA, Laxenburg, Austria
837 (http://www.iiasa.ac.at/research/LUC/External-World-Soil6database/HTML/).
838 Fekete, B. M., C. J. Vörösmarty, J. O. Road, and C. J. Willmott (2003), Uncertainties in
839 precipitation and their impacts on runoff estimates, J. Climate, 17, 294-304.

840 Frappart, F., F. Papa, A. Güntner, S. Werth, G. Ramillien, C. Prigent, W. B. Rossow, and M.-P.
841 Bonnet (2010), Interannual variations of the terrestrial water storage in the Lower Ob' basin
842 from a multisatellite approach. Hydrol. Earth Syst. Sci., 14, 2443-2453, doi:10.5194/hess-
843 14-2443-2010.
844 Gedney N., P. M. Cox, H. Douville, J. Polcher, and P. J. Valdes (2000) Characterizing GCM
845 land surface schemes to understand their responses to climate change. J. Climate, 13, 3066–
846 3079.
847 Gedney, N., P. M. Cox, and C. Huntingford (2004), Climate feedback from wetland methane
848 emission, Geophys. Res. Lett., 31, L20503, doi:10.1029/2004GL020919.
849 Güntner, A., J. Stuck, S. Werth, P. Döll, K. 757 Verzano, and B. Merz (2007), A Global
850 analysis of temporal and spatial variations in continental water storage, Water Resour. Res.,
851 43, W05416, doi:10.1029/2006WR005247.
852 Hagemann, S. and Dümenil, L (1998).: A parameterization of lateral water flow for the global
853 scale, Clim. Dyn., 14, 17–41.
854 Hansen, M. C., R. S. Defries, J. R. G. Townshend, and R. Sohlberg (2000) Global land cover
855 classification at 1 km spatial resolution using a classification tree approach. Int. J. Remote
856 Sensing, 21, 1331-1364.
857 Houweling, S., T. Kaminski, F. Dentener, J. Lelieveld, and M. Heinmann (1999) Inverse
858 modeling of methane sources and sinks using adjoint of a global transport model, J.
859 Geophys. Res., 104, 26 137-26 160.
860 Knighton, E., (1998), Fluvial forms and processes: A new perspective, London, Edward
861 Arnold, 383 p.

862 Koster, R.D., P.A. Dirmeyer, A.N. Hahmann, R. Ijpelaar, L. Tyahla, P. Cox, and M.J. Suarez
863 (2002) Comparing the Degree of Land–Atmosphere Interaction in Four Atmospheric
864 General Circulation Models. J. Hydrometeor., 3, 363–375.
865 Koster, R.D., Suarez M., Ducharne A., Stieglitz M. and Kumar P. (2000) A catchment-based
866 approach to modeling land surface processes in a GCM - Part 1: Model structure. J.
867 Geophys. Res., 105(D20):24809-24822.
868 Kouraev A., E. A.Zakharova, O. Samain, N. Mognard-Campbell and A. Cazenave (2004) Ob
869 river discharge from Topex/Poseidon satellite altimetry. *Remote Sensing of Environment*,
870 **93**, 238-245.
871 Krinner, G. (2003), Impact of lakes and wetlands on boreal climate, J. Geophys. Res., 108,
872 D16, 4520, doi:10.1029/2002JD002597.
873 Lawrence, D. M., and A. G. Slater (2007) Incorporating organic soil into a global climate
874 model. Climate Dynamics, 30(2-3), 145-160.
875 Leduc, C., J. Bromley and P. Schroeter (1997) Water table fluctuation and recharge in semi-
876 arid climate: some results of the HAPEX-Sahel hydrodynamic survey (Niger). J. of
877 Hydrology, 188-189, 123-138.
878 Leduc, C., G. Favreau and P. Schroeter (2001) Long term rise in a Sahelian water-table: the
879 continental terminal in South-West Niger. J. of Hydrology, 243, 43-54.
880 Lehner B. and Döll P. (2004) Developement and validation of a global database of lakes,
881 reservoirs and wetlands. J. of Hydrology, 296, 1-22.
882 Liston, G. E., Sud, C., and Wood, E. F. (1994) Evaluating GCM land surface hydrology
883 parameterizations by computing river discharges using a runoff routing model: application
884 to the Mississipi basin. *J. Appl. Meteorol.*, 33, 394-405.

885 Lucas-Picher, P., V.K. Arora, D. Caya, et R. Laprise (2003) Implementation of a large-scale
886 variable velocity flow routing algorithm in the Canadian Regional Climate Model (CRCM).
887 *Atmosphere-Ocean*, 41, 139-153.
888 Manning, R., (1891), On the flow of water in open channels and pipes, Institut of Civil
889 Engeneers of Ireland Transaction, 20, 161-207.
890 Masson V., J.-L. Champeaux, C. Chauvin, C. Meriguet, and R. Lacaze (2003) A global
891 database of land surface parameters at 1 km resolution for use in meteorological and climate
892 models. J. Climate, 16, 1261–1282.
893 Matthews, E. (2000), Wetlands, in Atmospheric methane: its role in the global environment,
894 edited by M. A. K. Khalil, pp. 202-233, Springer-Verlag, New York.
895 Miguez-Macho, G., Y. Fan, C.-P. Weaver, R. Walko, and A. Robock (2007) Incorporating
896 water table dynamics in climate modeling: 2. Formulation, validation, and soil moisture
897 simulation. *J. Geophys. Res.*, 112, D13108, doi: 10.1029/2006JD008112.
898 Miller, J. R., G. L. Russel, and G. Caliri (1994) Continental-scale river flow in climate models.
899 *J. Climate*, **7**, 914-928.
900 Molod, A., H. Salmun and D. Waugh, 2004: The Impact on a GCM Climate of an Extended
901 Mosaic Technique for the Land - Atmosphere Coupling. J. Climate, 17, 3877-3891.
902 Moody, J.A, and B.M. Troutman (2002), Characterization of the spatial variability of channel
903 morphology, Earth Surf. Process. Landforms, 27, 1251-1266.
904 Ngo-Duc, T., J. Polcher, and K. Laval (2005), A 53-year forcing data set for land surface
905 models, J. Geophys. Res., 110, D06116, doi:10.1029/2004JD005434.
906 Ngo-Duc, T., T. Oki, and S. Kanae (2007) A variable streamflow velocity method for global
907 river routing model: model description and preliminary results Hydrol. Earth Syst. Sci.
908 Discuss., 4, 4389–4414.

909 Noilhan J., and S. Planton (1989), A simple parameterization of land surface processes for
910 meteorological models, Mon. Wea. Rev., 117, 536-549.
911 Oki T., and Y. C. Sud (1998), Design of Total Runoff Integrating Pathways (TRIP). A global
912 river channel network, Earth Interaction, 2, 1-36.
913 Papa, F., C. Prigent, and W.B. Rossow (2007), Ob' River flood inundations from satellite
914 observations: A relationship with winter snow parameters and river runoff., J. Geophys.
915 Res., 112, D18103, doi:10.1029/2007JD008451.
916 Papa, F., C. Prigent, and W.B. Rossow (2008), Monitoring flood and discharge variations in
917 the large Siberian rivers from a multi-satellite technique. *Surv. Geophys.*, 29, 297-317,
918 doi:10.1007/s10712-008-9036-0
919 Papa, F., C. Prigent, F. Aires, C. Jimenez, W.B. Rossow, and E. Matthews (2010a) Interannual
920 variability of surface water extent at the global scale, 1993-2004. J. Geophys. Res., 115,
921 D12111, doi:10.1029/2009JD012674.
922 Papa, F., F. Durand, W.B. Rossow, A. Rahman, and S. Bala (2010b), Satellite altimeter-
923 derived monthly discharge of the Ganga-Brahmaputra River and its seasonal to interannual
924 variations from 1993 to 2008. *J. Geophys. Res*, 115, C12013, doi:10.1029/2009JC006075.
925 Portmann F.T., S. Siebert and P. Döll (2010) Global monthly irrigated and rainfed crop areas
926 around the year 2000: A new hight-resolution data set for agricultural and hydrological
927 modeling. Global Biogeochem. Cycles, 24, GB1011, doi:10.1029/2008GB003435.
928 Price, JS, Branfireum BA, Waddington JM, Devito KJ (2005) Advances in Canadian wetland
929 hydrology, 1999-2003. Hydrol. Process., 19, 201-214.
930 Prigent, C., E. Matthews, F. Aires, and W.B. Rossow (2001), Remote sensing of global
931 wetland dynamics with multiple satellite data set, Geophys. Res. Letters, 28, 4631-4634.

Prigent, C., F. Papa, F. Aires, W.B. Rossow, and E. Matthews (2007), Global inundation dynamics inferred from multiple satellite observations, 1993-2000, J. Geophys. Res., 112, D12107, doi:10.1029/2006JD007847.

Ringeval, B., N. de Noblet‐Ducoudré, P. Ciais, P. Bousquet, C. Prigent, F. Papa, and W. B. Rossow (2010), An attempt to quantify the impact of changes in wetland extent on methane emissions on the seasonal and interannual time scales, *Global Biochem. Cycles*, 24, GB2003, doi:10.1029/2008GB003354.

Roddel, M., Velicogna, I., and Famiglietti, J.S.: Satellite-based estimates of groundwater depletion in India, Nature, 460, 999-1003, doi:10.1038/nature08238, 2009.

Sacks W.J., B.I. Cook, N. Buenning, S. Levis and J.H Helkowski (2009) Effects of global irrigation on the near-surface climate. Clim. Dyn., 33, doi: 10.1007/s00382-008-0445-z.

Sheffield J., G. Goteti, and E. F. Wood (2006) Development of a 50-year high-resolution global data set of meteorological forcings for land surface modeling. J. Climate, 19, 3088–3111.

Shindell, D. T., G. Falugevi, N. Bell, and G. A. Schmidt (2004), An emission-based view of climate forcing by methane and tropospheric ozone, Geophys. Res. Lett., 32, doi:10.1029/2004GL021900.

Thomas, H., and T.R. Nisbet (2006), An assessment of the impact of floodplains woodland on flood flow, Water and Environement J., 21, 114-126.

Verdin K.L. and S.K. Greenlee (1996) Development of continental scale digital elevation models and extraction of hydrographic features. In: Proceedings, Third International Conference/Workshop on Integrating GIS and Environmental Modeling, Santa Fe, New Mexico, January 21-26, 1996, National Center for Geographic Information and Analysis, Santa Barbara, California.

956 Vörösmarty, C. J., B. Moore, A. L. Grace, M. P. Gildea, J. M. Melillo, B. J. Peterson, E. B.
957 Rastetter, and P. A. Steudler (1989) Continental scale models of water balance and fluvial
958 transport : an application to South America. *Global Biogeochemical Cycles*, **3**, 241-265.

TABLE CAPTIONS

TABLE 1 - Examples of river basin characteristics in the TRIP 1° by 1° network. The basin name, the basin drainage area (*Area* in km²), the locations (longitude, *Lon*, and latitude, *Lat*), the basin β coefficient (Equation 8), and the width (m) are given. The different values of the bankfull height at each river mouth are also shown.

Basins	*Area (km²)*	*Lon*	*Lat*	*β*	*Width (m)*	h_c *(m)*	h_c *-25%*	h_c *+25%*
Amazon	6 134 937	-50.5	0.5	32	14755	25	18.75	31.25
Congo	3 751 344	12.5	-5.5	32	6860	19	14.25	23.75
Mississippi	3 245 654	-90.5	29.5	15	2 112	13	9.75	16.25
Parana	3 007 044	-58.5	-34.5	20	2872	14	10.5	17.5
Nile	2 961 360	30.5	30.5	32	2 511	14	10.5	17.5
Ob	2 958 911	70.5	66.5	25	2 936	14	10.5	17.5
Yenisei	2 603 497	83.5	71.5	25	3 658	15	11.25	18.75
Lena	2 335 590	124.5	73.5	25	2 934	14	10.5	17.5
Niger	2 119 052	6.5	5.5	20	1531	12	9	15
Amur	1 864 936	140.5	53.5	15	1 700	12	9	15
Yangtze	1 827 110	120.5	31.5	20	3 679	15	11.25	18.75
Mackenzie	1 736 363	-134.5	68.5	25	2 520	14	10.5	17.5
Volga	1 387 236	48.5	46.5	25	2 242	13	9.75	16.25
Murray	1 067 251	-35.5	139.5	15	594	8	6	10
Ganges	1 029 593	88.5	22.5	20	2 521	14	10.5	17.5
Orinoco	958 945	-61.5	9.5	32	5 621	18	13.5	22.5
Yukon	844 111	-164.5	62.5	25	2 299	13	9.75	16.25
Danube	804 386	29.5	45.5	15	1 597	12	9	15
Mekong	801 386	106.5	10.5	20	2 706	14	10.5	17.5
Sénégal	429 686	16.5	-15.5	20	575	8	6	10
Loire	118 046	-1.5	47.5	15	541	8	6	10
Rhône	95 461	4.5	44.5	15	694	9	6.75	11.25

TABLE 2 - The 12 vegetation types specified according to the 1-km ECOCLIMAP data base and the corresponding floodplain roughness coefficient, n_i, used in Equation 10.

	Vegetation types	***Floodplain roughness coefficient***
1	Bare soil	0.035
2	Rocks	0.035
3	Permanent snow and ice	0.035
4	Forest and trees	0.075
5	Coniferous forest	0.100
6	Broadleaf evergreen forest	0.100
7	C3 crops	0.050
8	C4 crops	0.050
9	Irrigated crops	0.050
10	Grassland	0.050
11	Tropical grassland	0.075
12	Peat bogs and Irrigated grass	0.075

FIGURES AND CAPTIONS

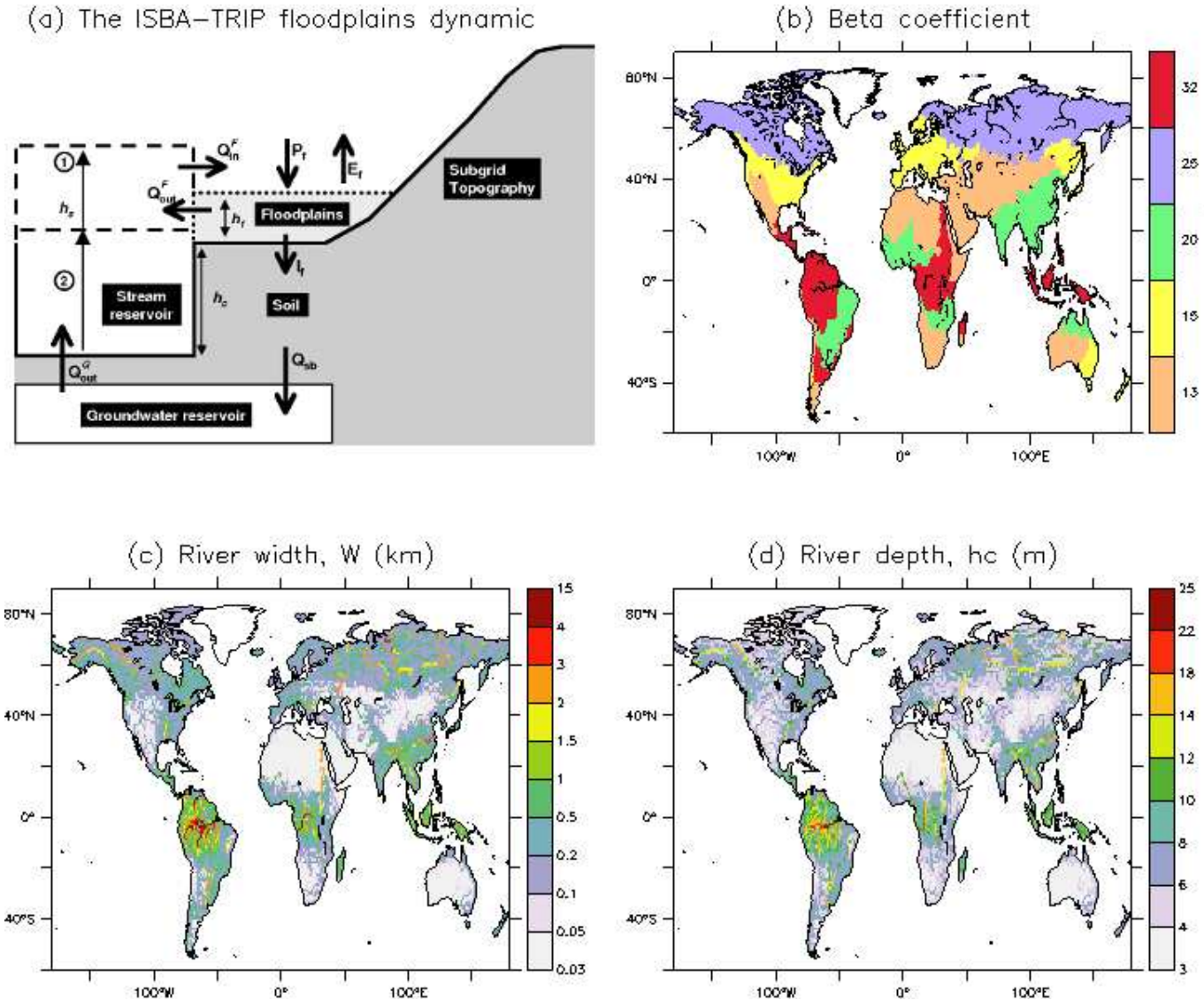

Figure 1 – The ISBA-TRIP floodplain dynamics and the Global distribution of its specific parameters. (a) Schematic representation: (case 1) when the river depth, h_s, is above the critical river bankfull height, h_c, a flood inflow, Q_{in}^{F}, is computed; (case 2) when the flood decreases, h_s becomes lower than the depth of the floodplains, h_f, and a flood outflow, Q_{out}^{F}, to the river is computed. See section 2 for more details. (b) The β coefficient used to compute the river width given in (c). (d) The bankfull river height. See section 3 for more details.

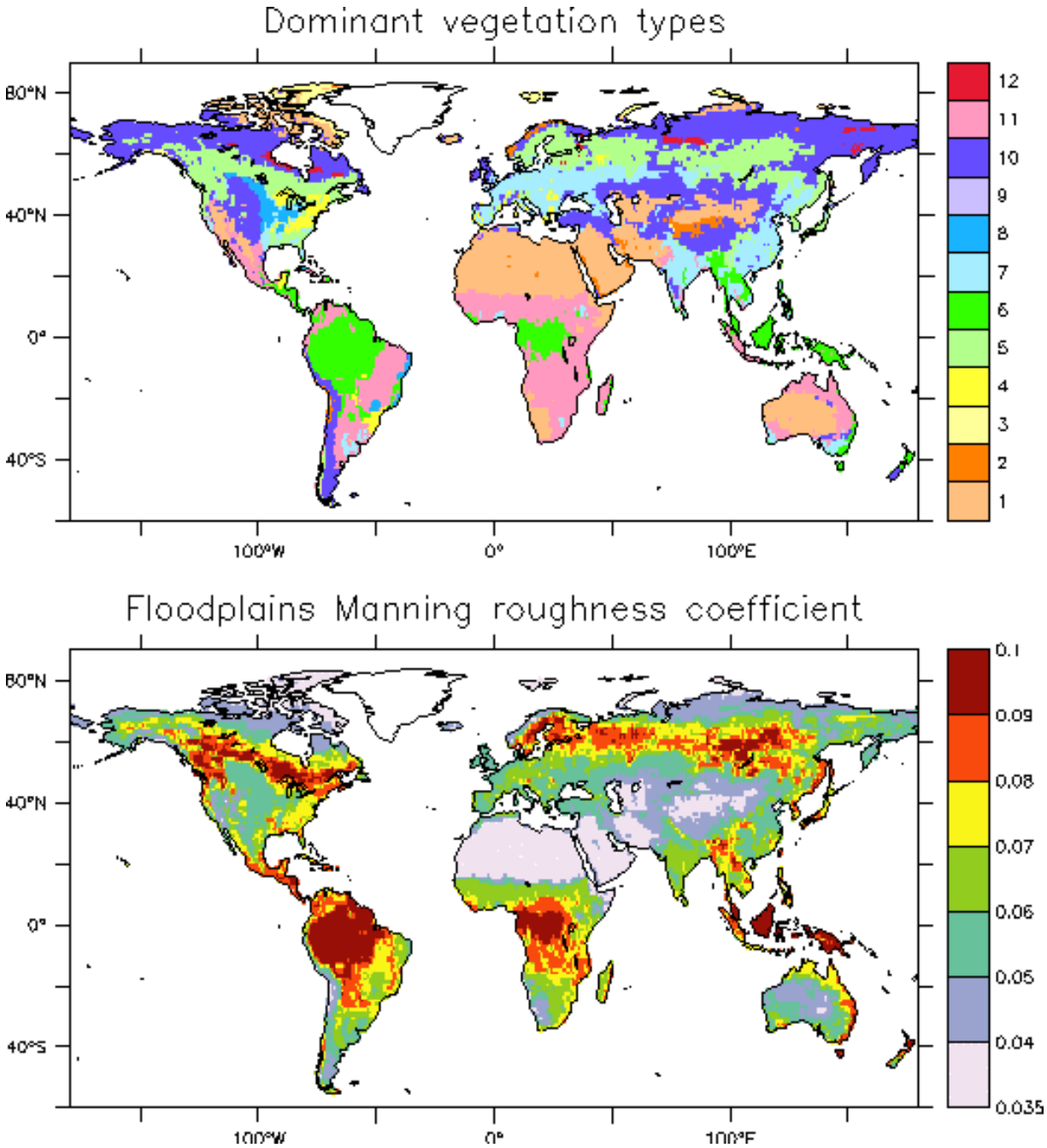

Figure 2 – Spatial distribution of the dominant vegetation types at 1° resolution specified according to the 1-km ECOCLIMAP data (top) and the associated floodplain Manning roughness coefficient (bottom). The 12 vegetation types are described in Table 2.

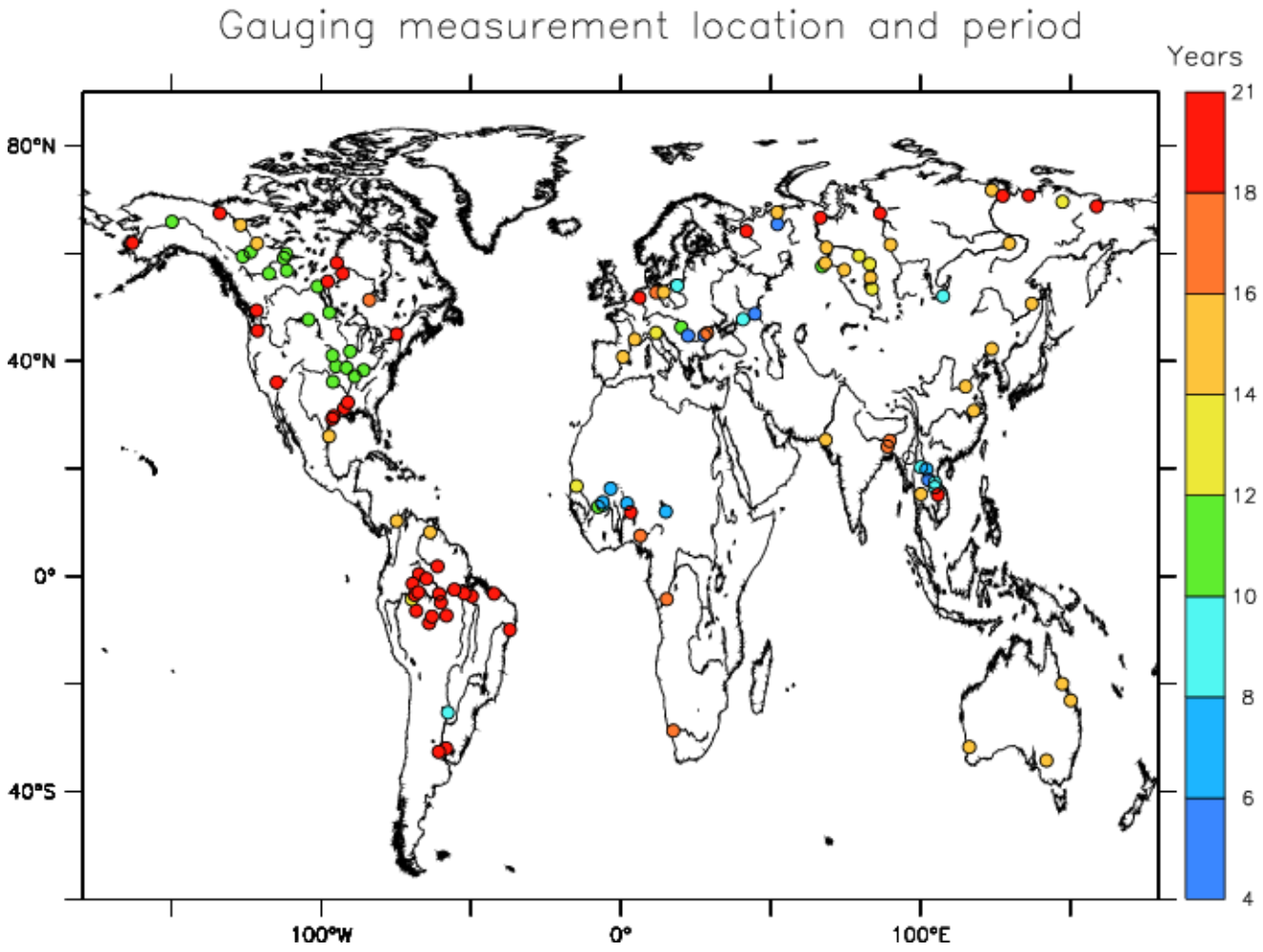

Figure 3 – Location of the 122 gauging stations used for the evaluation. The color on each station represents the number of year of monthly data available, beginning in January 1986.

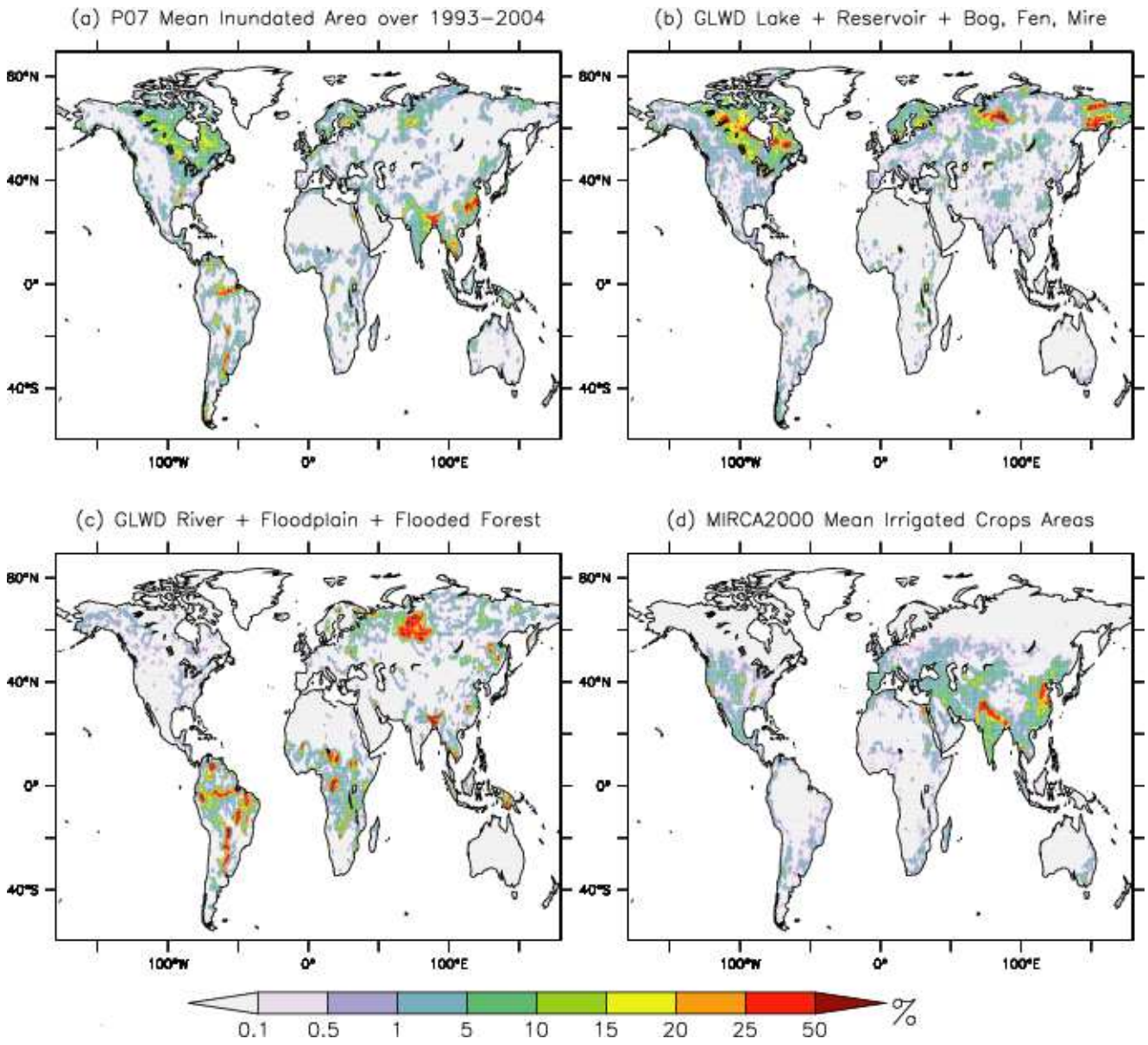

Figure 4 – The different data sets used for the floodplain evaluation. (a) The global distribution of the P07 1993-2004 mean inundated extent. (b) The lakes, reservoirs, bogs, fens and mires from the GLWD database. (c) The GLWD rivers, floodplains and flooded forest areas. (d) The MIRCA2000 mean irrigated crop extent.

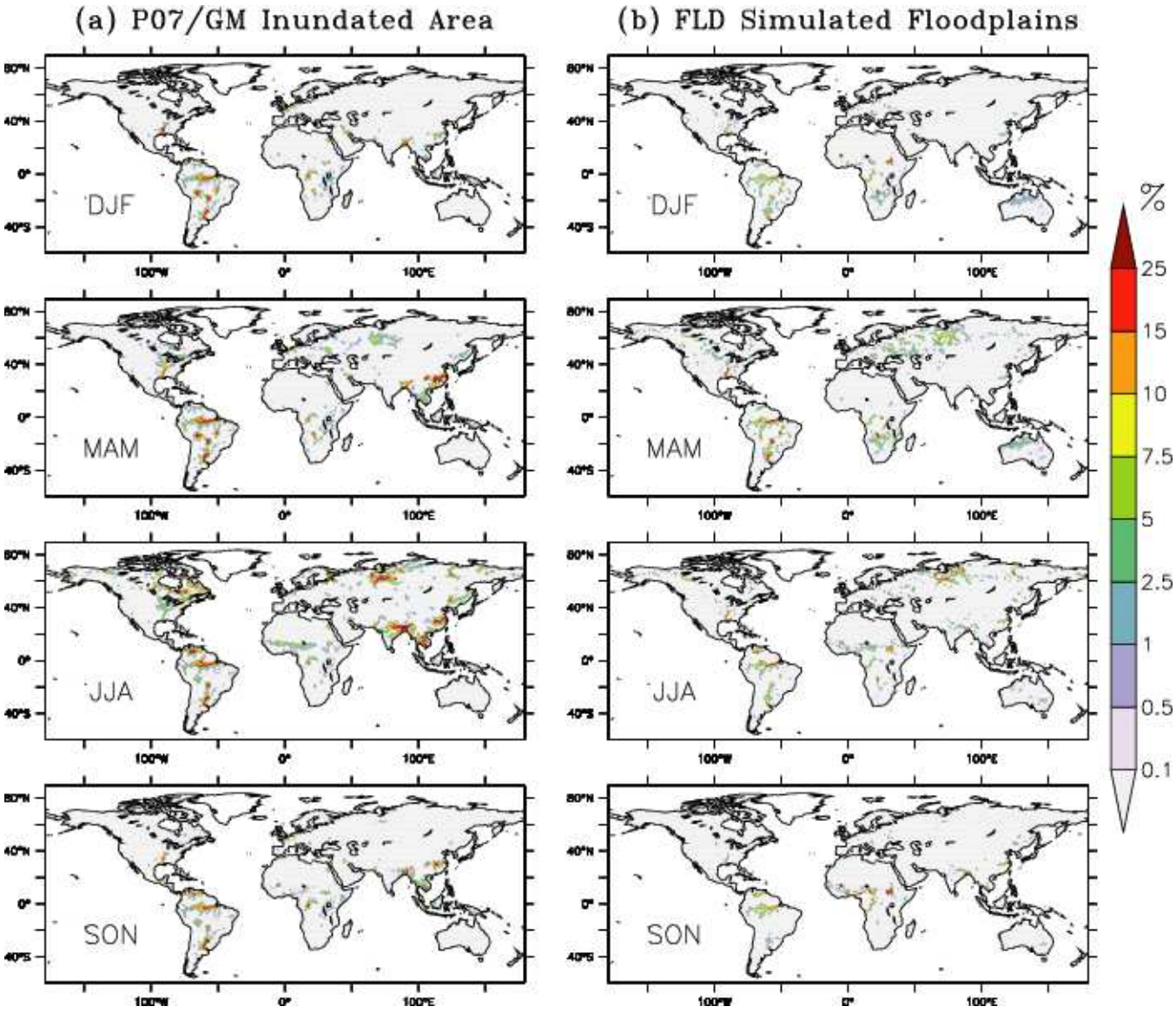

Figure 5 – Spatial distribution of the mean annual cycles of both the $P_{07/GM}$ inundated areas (b) and the simulated FLD floodplains.

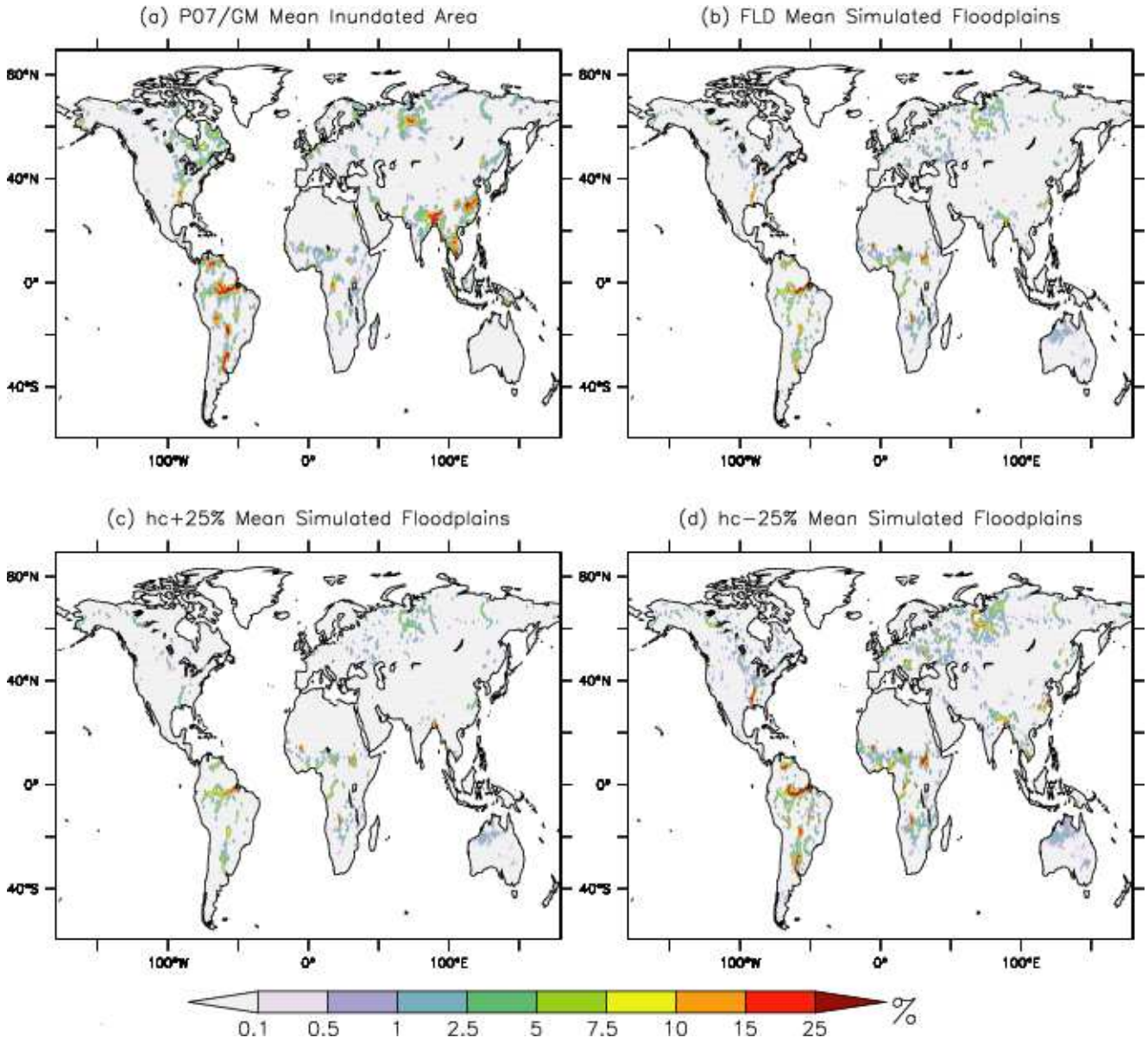

Figure 6 – Spatial distribution of the annual mean inundated areas estimated by $P_{07/GM}$ (a), simulated by FLD (b), and computed with h_c±25% (c and d).

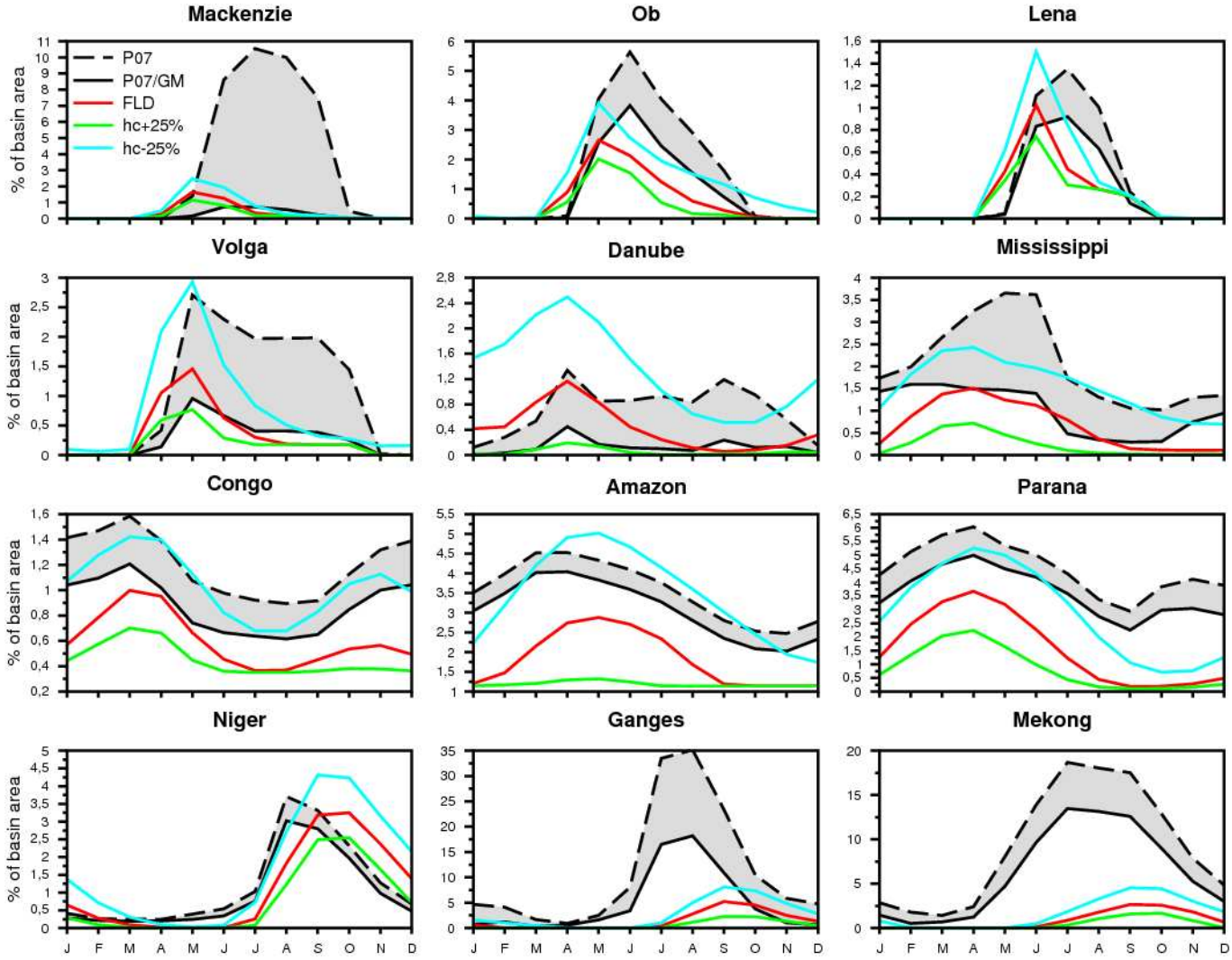

Figure 7 – Comparison over major river basins between the basin-averaged annual cycles of simulated and estimated flooded areas over the 1993-2004 period. P07 is in dashed black line, $P_{07/GM}$ in black, FLD in red, and $h_c \pm 25\%$ in green and cyan. Note that the maximum value on the Y-axis is highly variable from one basin to the other.

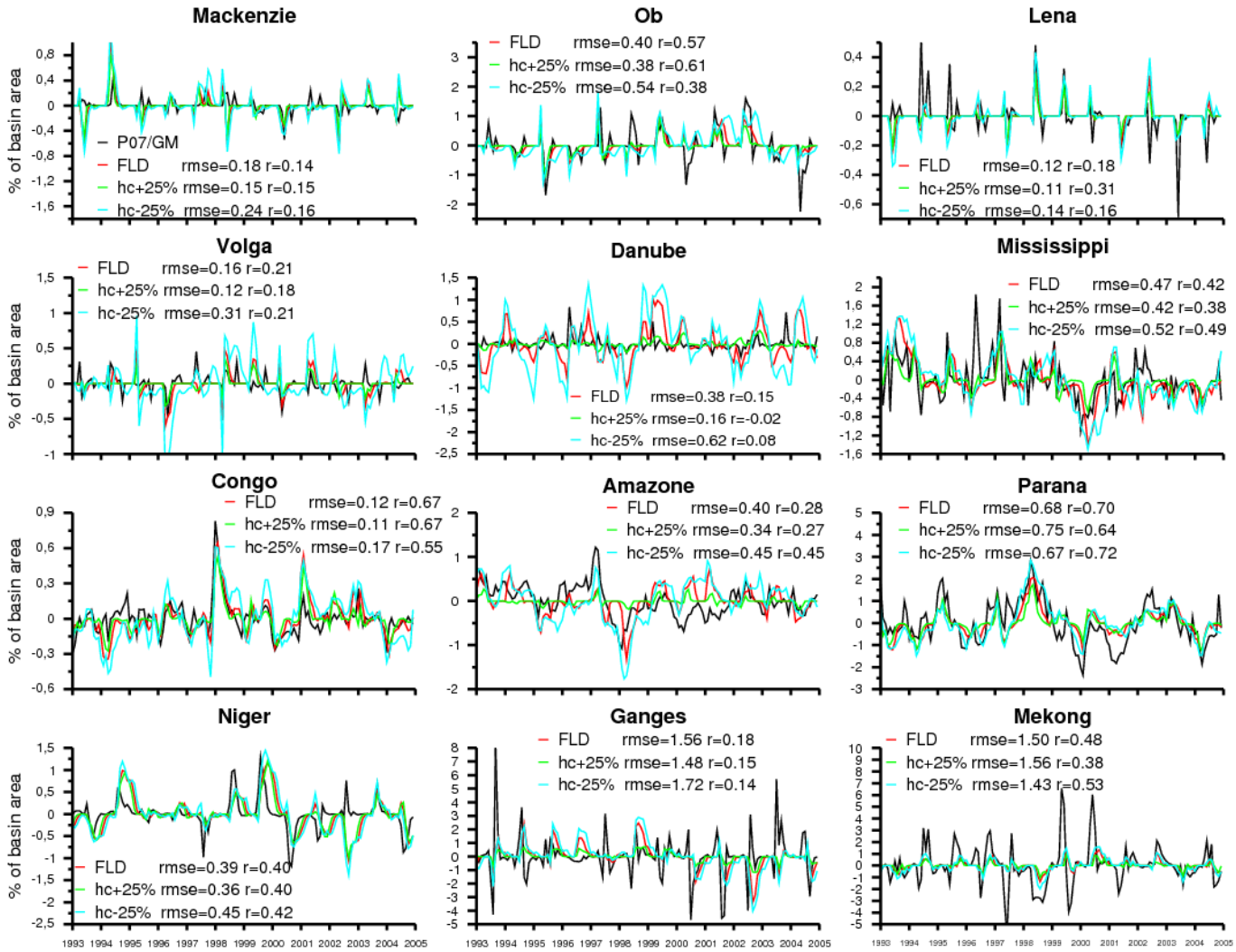

Figure 8 – Comparison between the major basin-averaged simulated and estimated (black line) floodplain anomalies over the 1993-2004 period. The Root Mean Square Error (RMSE) and the correlation (r) are given for each simulation. Notations are the same than in Figure 7.

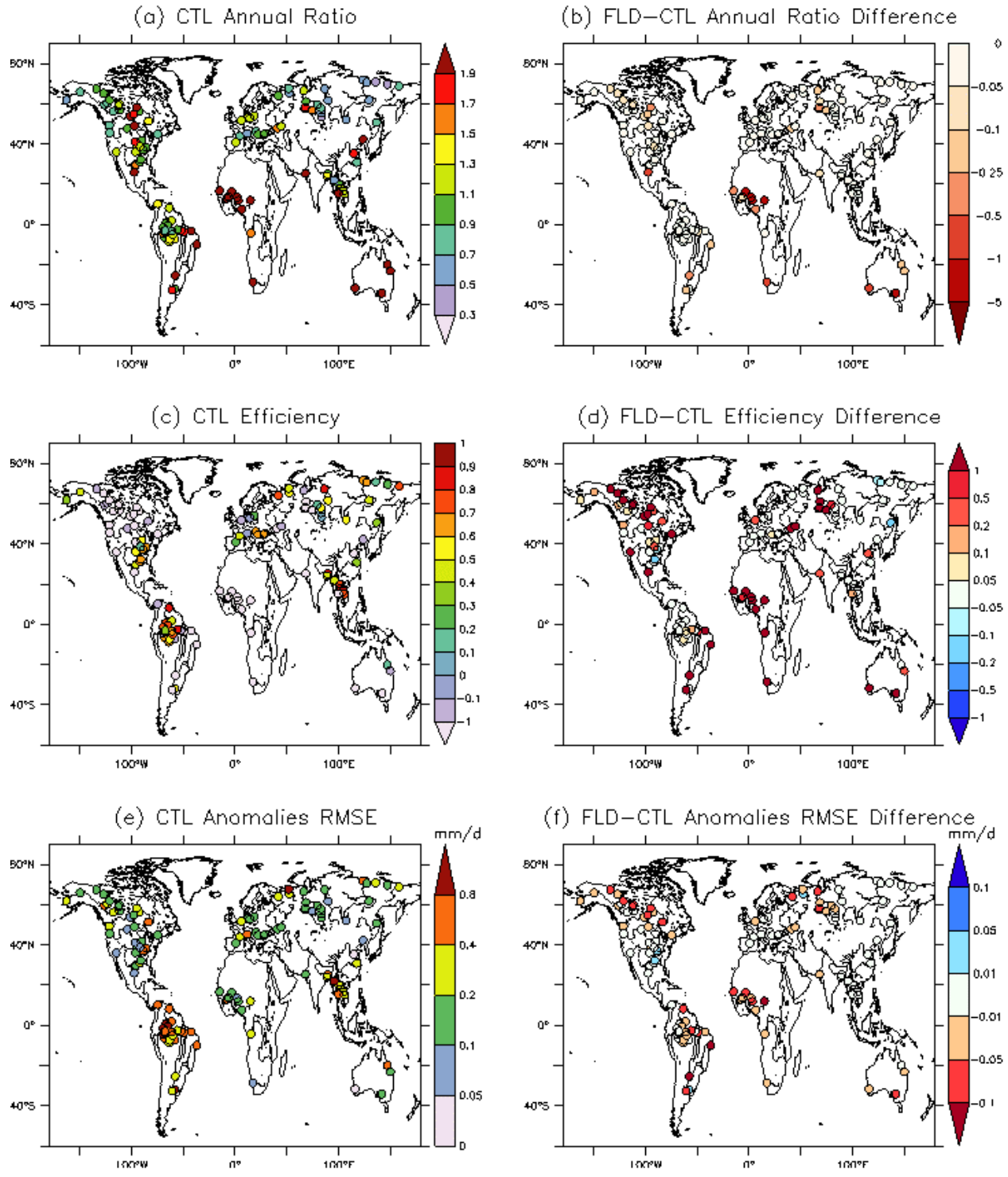

Figure 9 – Comparison between the simulated monthly discharge with (FLD) and without (CTL) the flood scheme at each 122 gauging station. The CTL annual ratio (a) and efficiency

(c) in terms of absolute values as well as the RMSE in terms of monthly anomalies (e) are given. The difference with the FLD scores is also shown (b, d, f).

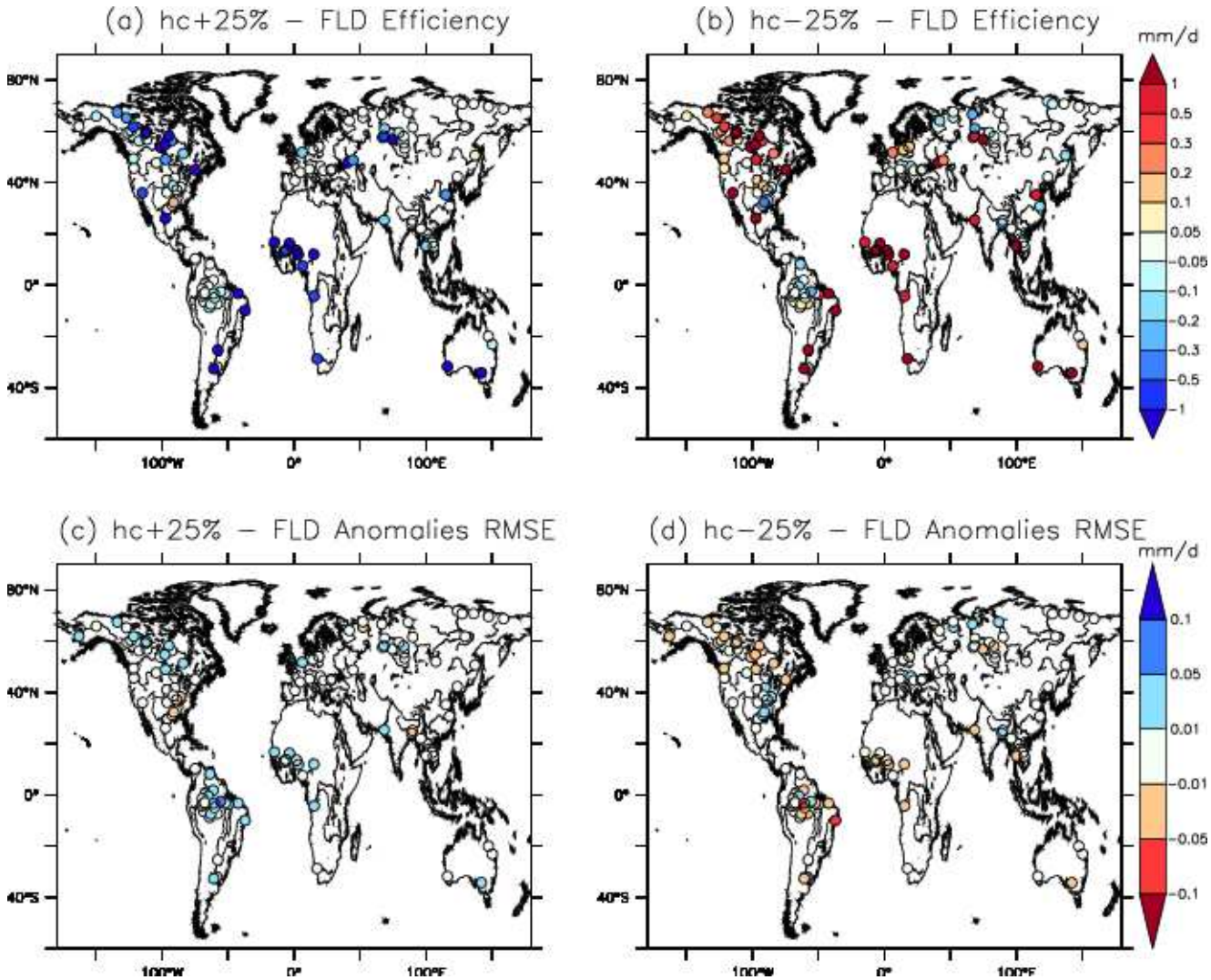

Figure 10 – Sensitivity of the simulated monthly discharge to the river bankfull height at each 122 gauging station. The difference between simulations with h_c±25% and FLD is given in terms of efficiency (a, b), and monthly anomalies RMSE (c, d).

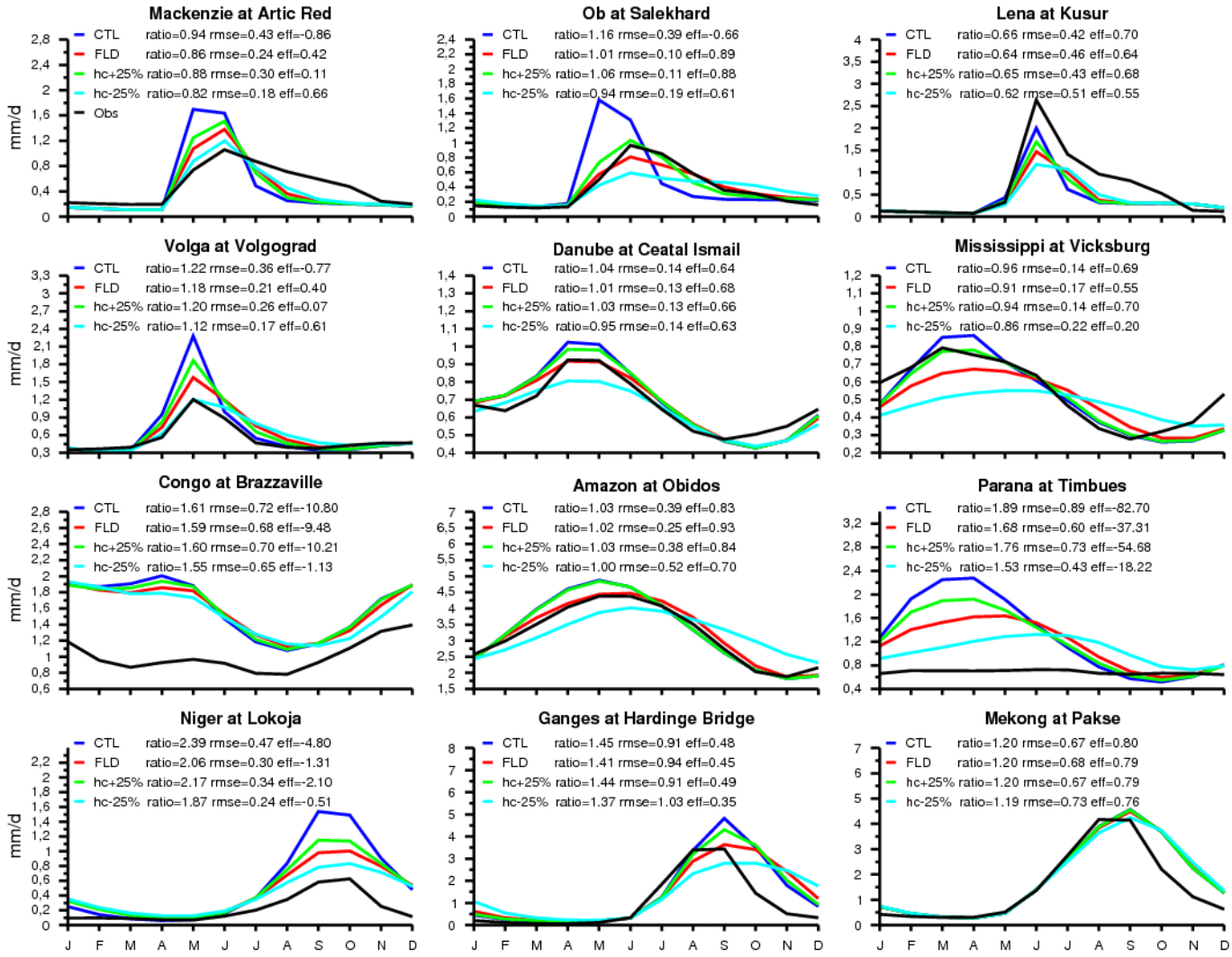

Figure 11 – Comparison between the mean annual cycles of simulated and observed (black line) discharges over the same basins than in Figure 7. Observations are in black line, CTL in blue, FLD in red, and h_c±25% in green and cyan. The ratio, RMSE, and efficiency (eff) criteria given on each panel are calculated over the entire period and not over the annual cycle.

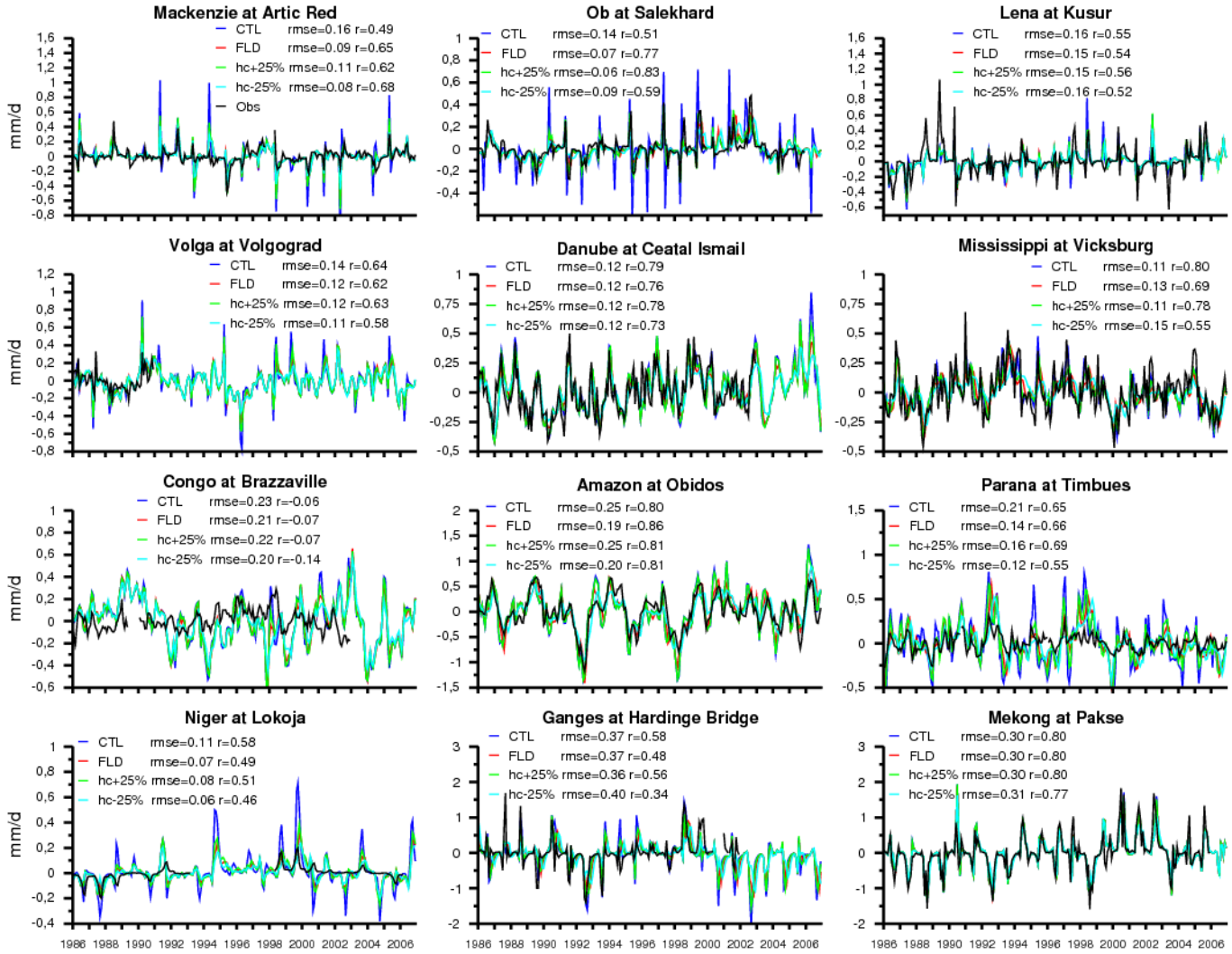

Figure 12 – Same as in Figure 10 but for the interannual variability. The RMSE and the correlation (r) are given for each experiment.

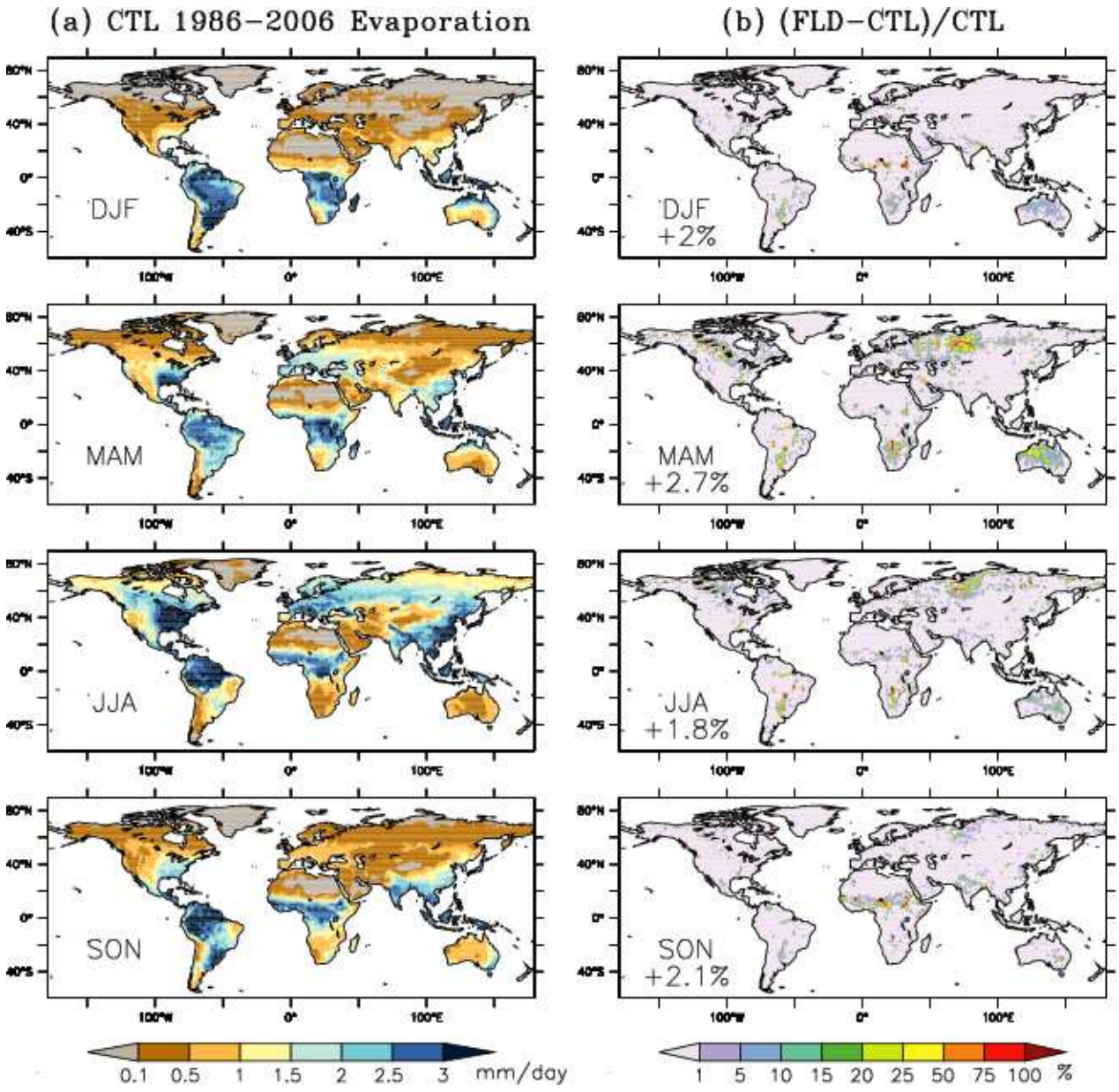

Figure 13 – Impact of the flood scheme on the evapotranspiration mean annual cycle computed by ISBA over the 1986-2006 period. (a) Global distribution of the CTL evapotranspiration. (b) Comparison in % between CTL and FLD.

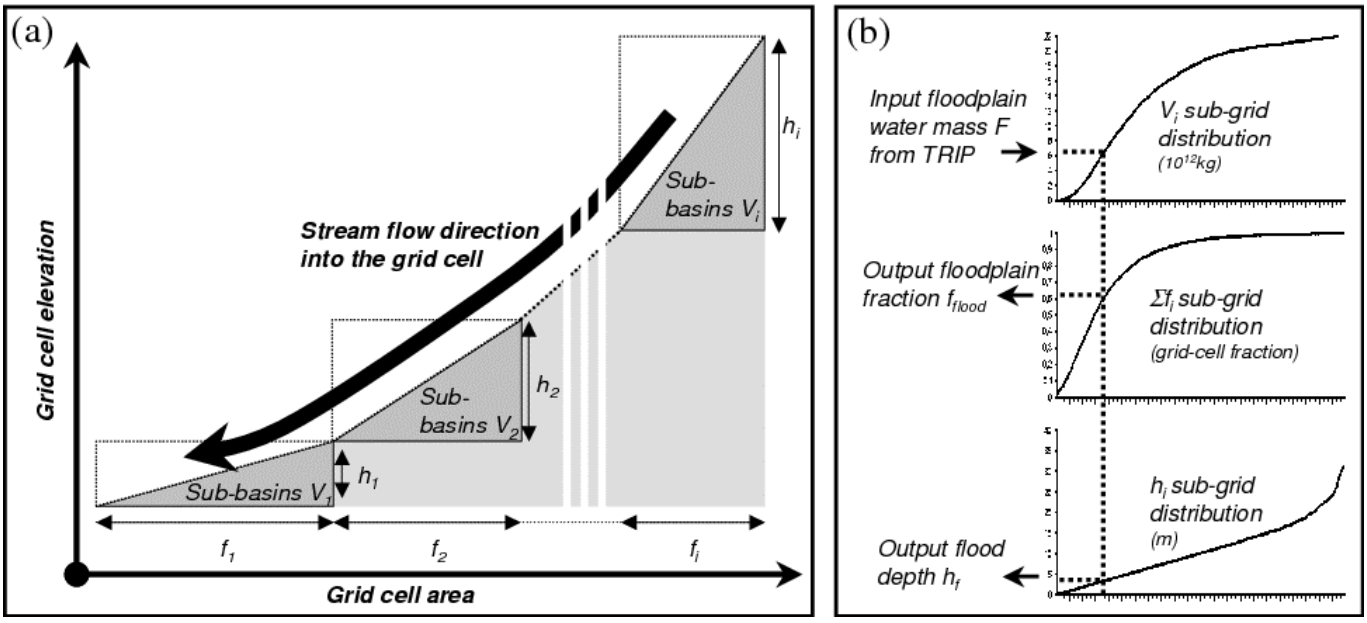

Figure 14 – Schematic representation of the floodplain sub-grid scheme. (a) One grid-cell is approximated as an individual basin where the water flows from the largest to the flattest slope of each pixel at 1 km resolution. Each pixel is then assumed as a sub-basin that can be potentially flooded. These pixels are ranked from the lower to the higher depth, h_i, computed according to the slope of each pixel. Then, a sub-grid area, f_i, and a potential water mass, V_i, can be associated with each entity. (b) The comparison of the floodplain water mass, F, computed by TRIP with the V_i sub-grid distribution permits to find the associated floodplain fraction, f_{flood}, and flood depth, h_f, into the grid cell via the sub-grid distribution of f_i and h_i respectively.